J. Fluid Mech. (2012), *vol.* 699, *pp.* 1–49. © Cambridge University Press 2012
doi:10.1017/jfm.2011.560

Low-frequency unsteadiness in shock wave–turbulent boundary layer interaction

Stephan Priebe[1,2] **and M. Pino Martín**[2]†

[1] Department of Mechanical and Aerospace Engineering, Princeton University, Princeton, NJ 08544, USA
[2] Department of Aerospace Engineering, University of Maryland, College Park, MD 20742, USA

(Received 7 March 2011; revised 14 December 2011; accepted 19 December 2011;
first published online 24 April 2012)

The low-frequency unsteadiness is characterized in the direct numerical simulation of a shock wave–turbulent boundary layer interaction generated by a 24° compression ramp in Mach 2.9 flow. Consistent with experimental observations, the shock wave in the simulation undergoes a broadband streamwise oscillation at frequencies approximately two orders of magnitude lower than the characteristic frequency of the energetic turbulent scales in the incoming boundary layer. The statistical relation between the low-frequency shock motion and the upstream and downstream flow is investigated. The shock motion is found to be related to a breathing of the separation bubble and an associated flapping of the separated shear layer. A much weaker statistical relation is found with the incoming boundary layer. In order to further characterize the low-frequency mode in the downstream separated flow, the temporal evolution of the low-pass filtered flow field is investigated. The nature of the velocity and vorticity profiles in the initial part of the interaction is found to change considerably depending on the phase of the low-frequency motion. It is conjectured that these changes are due to an inherent instability in the downstream separated flow, and that this instability is the physical origin of the low-frequency unsteadiness. The low-frequency mode observed here is, in certain aspects, reminiscent of an unstable global mode obtained by linear stability analysis of the mean flow in a reflected shock interaction (Touber & Sandham, *Theor. Comput. Fluid Dyn.*, vol. 23, 2009, pp. 79–107).

Key words: boundary layer separation, shock waves, turbulent boundary layers

1. Introduction

Shock wave–turbulent boundary layer interactions (STBLIs) occur in many external and internal compressible flow applications such as transonic aerofoils, high-speed engine inlets, internal flowpaths of scramjets, over-expanded rocket engine nozzles and deflected control surfaces or any other discontinuities in the surface geometry of high-speed vehicles. STBLIs are of engineering interest and an important factor in vehicle development since large-scale unsteady flow separation can occur in the interaction, which deteriorates the quality of the flow downstream, and since the interaction can cause strong fluctuations of pressure and heat transfer at the surface (Délery & Marvin 1986; Dolling 2001; Smits & Dussauge 2006; Clemens & Narayanaswamy 2009).

† Email address for correspondence: pmartin@umiacs.umd.edu

https://doi.org/10.1017/jfm.2011.560 Published online by Cambridge University Press

The parameter that governs the interaction at fixed Reynolds number, Mach number and wall temperature condition is the interaction strength, i.e. the pressure rise that is imposed on the boundary layer, which is set, for example, in a compression ramp flow by means of the ramp angle and in a reflected shock flow by adjusting the angle of the incident shock. As the strength of the interaction is increased, mean flow separation develops: in mild interactions, the flow is fully attached; in intermediate-strength interactions, it is incipiently separated, i.e. no separation occurs in the mean but the probability of observing reversed flow instantaneously is significant; in strong interactions, the flow is separated in the mean, and the length of separated flow increases with further increases in the interaction strength. The development of mean flow separation with increasing interaction strength and the associated changes in the flow topology are treated in many references – see e.g. Settles, Fitzpatrick & Bogdonoff (1979) for the compression ramp case and Green (1970) for the reflected shock case.

In addition to mean flow separation developing with increasing interaction strength, an unsteadiness at frequencies much lower than the characteristic frequency of the energetic eddies in the incoming boundary layer appears. For strong interactions, power spectra in the shock motion region show, in addition to the broadband bump associated with the turbulence, a second broadband bump at much lower frequencies – see, among many other references, Ringuette *et al.* (2009) for the compression ramp case and Dupont, Haddad & Debiève (2006) for the reflected shock case. The characteristic frequency of the turbulence in the incoming boundary layer is $O(U_\infty/\delta)$, whereas the frequency of the low-frequency unsteadiness is $O(0.01U_\infty/\delta)$, where U_∞ is the free stream velocity and δ is the boundary layer thickness based on 99 % of U_∞. The physical origin of the low-frequency shock motion is under debate. Previous works have correlated the low-frequency shock motion with fluctuations in the incoming boundary layer (upstream influence) or the separated flow (downstream influence), and differing conclusions have been drawn as to whether the shock motion is caused by a low-frequency mechanism in the upstream or downstream flow.

Concerning upstream influences on the shock motion, Beresh, Clemens & Dolling (2002) found in a Mach 5 compression ramp interaction that streamwise velocity fluctuations in the upstream boundary layer are correlated with the shock motion. They proposed that the shock motion is caused by continuous variations in the upstream velocity profile with a momentarily fuller profile, which is more resistant to separation, resulting in downstream shock motion, and a momentarily less full profile, which is less resistant to separation, resulting in upstream shock motion. Ganapathisubramani, Clemens & Dolling (2007, 2009) investigated the role of very long regions of low and high momentum in the incoming boundary layer as an upstream source of low-frequency unsteadiness. These superstructures, which are known from incompressible flows (e.g. Hutchins & Marusic 2007), have also been observed in compressible turbulent boundary layers (Ganapathisubramani, Clemens & Dolling 2006; Ringuette, Wu & Martín 2008*b*). The superstructures are a possible source of low-frequency unsteadiness since their streamwise length scale is at least $O(10\delta)$ and probably much longer. Ganapathisubramani *et al.* (2007, 2009) found that, in a Mach 2 compression ramp interaction, the upstream envelope of the separation region conforms to the elongated low- and high-speed regions present in the upstream boundary layer and that, in addition, global changes in the upstream velocity are correlated with spanwise-uniform motions of the separation region. They concluded that the low-frequency unsteadiness is caused by the upstream boundary layer and the passage of superstructures through the interaction. A correlation between the shock

https://doi.org/10.1017/jfm.2011.560 Published online by Cambridge University Press

and the upstream boundary layer has also been observed by Humble *et al.* (2009*a*) based on tomographic particle image velocimetry (PIV) measurements in a Mach 2.1 reflected shock interaction.

Concerning downstream influences on the shock motion, several works have found, based on unsteady wall pressure measurements, that fluctuations near the foot of the shock are correlated and out of phase with fluctuations beneath the downstream part of the separation bubble – see Erengil & Dolling (1991) in a Mach 5 compression ramp interaction, Thomas, Putnam & Chu (1994) in Mach 1.5 compression ramp interactions, and Dupont *et al.* (2006) in Mach 2.3 reflected shock interactions. A relation between the shock and the separation bubble has also been observed inside the flow based on PIV measurements: Piponniau *et al.* (2009) found that the position of the shock, conditioned on the size of the separation bubble, is more upstream for large bubbles and more downstream for small bubbles, and they concluded that pulsations of the bubble are related to movements of the shock. Similar results have been found in the direct numerical simulation (DNS) of a Mach 2.9 compression ramp interaction by Wu & Martín (2008) with motions of the shock and separation bubble correlated.

In addition to these statistical results, a physical model for the low-frequency unsteadiness has been proposed based on the properties of fluid entrainment by the shear layer formed downstream of the separation shock (Piponniau *et al.* 2009). According to the proposed scenario, the separated shear layer entrains mass from the separation bubble, causing a gradual depletion of the bubble until fresh reversed flow is supplied from downstream. This process, it is suggested, results in large-scale breathing of the bubble, which drives the shock motion. Treating the separated shear layer as a mixing layer, Piponniau *et al.* (2009) estimated the time scale of the bubble depletion by mass entrainment. This time scale was found to be consistent with the unsteadiness time scale observed in several STBLI flows and incompressible separated flows. The model explains the significant difference between the unsteadiness time scale observed in incompressible separated flows on the one hand and STBLI flows on the other by the dependence of the mixing layer spreading rate on Mach number.

Another possible mechanism is that an inherent instability in the separated flow is at the origin of the unsteadiness. Based on large eddy simulation (LES) data for a Mach 2.3 reflected shock interaction, Touber & Sandham (2009) performed a linear stability analysis of the mean flow and found an unstable global mode, which could be related to the low-frequency unsteadiness.

The objective of the present work is to characterize the low-frequency unsteadiness in the DNS of a Mach 2.9 compression ramp STBLI. Spectral and statistical methods are used to show which flow regions participate in the low-frequency unsteadiness and how these regions are statistically linked to the shock motion (see § 3.2). This part of the analysis is similar to the analysis by Dupont *et al.* (2006) of experimental wall pressure measurements in reflected shock interactions, but in the present work the spectral and statistical analysis is extended from the wall into the flow to give a time-resolved description of the unsteadiness in the entire flow field. The unsteadiness is similar in the reflected shock configuration (for which many of the recent results on the characterization of the unsteadiness have been obtained) and the compression ramp configuration, since the scalings of the unsteadiness frequency by Dussauge, Dupont & Debiève (2006) and Piponniau *et al.* (2009) collapse data from several configurations, including the reflected shock and compression ramp configurations, relatively well. The present compression ramp data are used to show similarities with previous results on the unsteadiness obtained in the reflected shock configuration and to highlight possible differences between the two configurations. The principal objective of the

https://doi.org/10.1017/jfm.2011.560 Published online by Cambridge University Press

present work is to provide a description of the low-frequency mode in the flow downstream of separation, including nonlinear effects, based on time-resolved data in the flow field, and involving the evolution of all relevant flow regions (the shock, separation bubble, separated shear layer and possibly the incoming boundary layer). From previous work, elements of this low-frequency mode are known: as mentioned above, Dupont *et al.* (2006) have shown that low-frequency pulsations of the wall pressure beneath the separation bubble are statistically linked to the shock motion; and Piponniau *et al.* (2009) have shown that instantaneously the size of the separation bubble is statistically linked to the shock position. In addition, Touber & Sandham (2009) have shown an unstable global mode in the separated flow from linear stability analysis, and this could be related to the low-frequency unsteadiness. To characterize the low-frequency mode in the DNS, the low-frequency evolution of the flow field is investigated from filtered DNS data in §§ 3.4 and 3.5. Based on the observations, the physical origin of the low-frequency unsteadiness is discussed in § 4.

2. Numerical method and computational set-up

2.1. *Governing equations and numerical discretization*

The full three-dimensional unsteady Navier–Stokes equations in conservation form are solved for a perfect gas. The equations are expressed in dimensionless form and in a curvilinear coordinate system. The usual constitutive relations for a Newtonian fluid are used: the viscous stress tensor is linearly related to the rate-of-strain tensor, and the heat flux vector is linearly related to the gradient of temperature through Fourier's law of heat conduction. The coefficient of viscosity μ is computed from Sutherland's law, and the coefficient of thermal conductivity is computed from $k = \mu c_p/Pr$, where the molecular Prandtl number is taken to be 0.74. A detailed presentation of the governing equations may be found in Wu & Martín (2007).

The governing equations are solved using a fourth-order weighted essentially non-oscillatory (WENO) scheme to discretize the inviscid fluxes. Compared with the original finite-difference WENO scheme introduced by Jiang & Shu (1996), which is too dissipative for the accurate and efficient computation of STBLI flows, the present scheme is modified in two respects. The first modification concerns the linear part of the scheme, that is, the scheme in smooth flow regions where a set of optimal WENO weights is engaged. The modification consists in adding a fully downwinded candidate stencil, which gives a symmetric collection of candidate stencils, and in optimizing the WENO weights to maximize bandwidth-resolving efficiency (Martín *et al.* 2006). The resulting symmetric bandwidth-optimized WENO scheme is still too dissipative for the accurate and efficient simulation of STBLI flows (Wu & Martín 2007). To reduce numerical dissipation further, the adaptation of the scheme away from the optimal weights in the presence of discontinuities (the nonlinear part of the scheme) is modified by means of limiters (Taylor, Wu & Martín 2007; Wu & Martín 2007). An absolute limiter on the WENO smoothness measurement and a relative limiter on the total variation are used together, and the expressions for the limiters and the threshold values are given in Wu & Martín (2007, equations (12) and (17)).

For the discretization of the viscous fluxes, standard fourth-order central differences are used, and time integration is performed by means of a third-order low-storage Runge–Kutta method (Williamson 1980).

The DNS code has been validated in previous work for supersonic shock wave–turbulent boundary layer interactions (Wu & Martín 2007; Priebe, Wu & Martín 2009). The DNS by Wu & Martín (2007) of supersonic flow over a compression

https://doi.org/10.1017/jfm.2011.560 Published online by Cambridge University Press

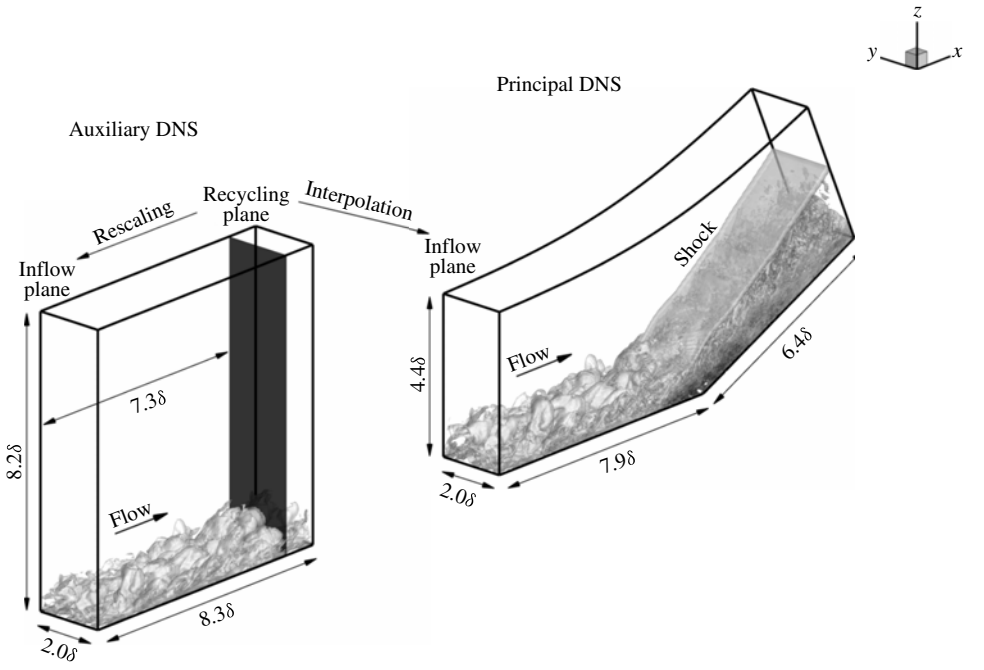


FIGURE 1. Computational domain and strategy for prescribing the inflow boundary condition. The reference length δ is the thickness of the boundary layer (based on 99 % of the free stream velocity) at the inflow plane of the principal DNS. An instantaneous flow field is shown in the domain, visualized by an isosurface of the magnitude of density gradient, $|\nabla\rho|\delta/\rho_\infty = 2.5$. The isosurface is shaded by the streamwise velocity component (with levels from $-0.4U_\infty$ to U_∞, black to white). Note that x, y and z are, respectively, the streamwise, spanwise and wall-normal coordinates.

ramp shows good agreement with experiments at matching flow conditions (see also Ringuette, Wu & Martín 2008*a*; Ringuette *et al.* 2009).

2.2. *Auxiliary and principal direct numerical simulation*

In addition to the DNS code being identical in the present simulation and the previous compression ramp simulation by Wu & Martín (2007), the general computational set-up (domain, grid, initial and boundary conditions) is also identical, except for differences in the treatment of the inflow boundary condition. In the previous simulation (Wu & Martín 2007), the inflow boundary condition was specified by the recycling–rescaling technique developed by Xu & Martín (2004), and the rescaling was performed as part of the principal simulation. In the present simulation, the recycling–rescaling technique by Xu & Martín (2004) is still used but we choose to perform the rescaling as part of an auxiliary boundary layer computation. The reason for detaching the rescaling from the principal simulation and performing an auxiliary simulation is the possibility of reusing the inflow data for other STBLI simulations and the associated savings in computational cost. Figure 1 shows the general set-up for the DNS in the present work. The auxiliary DNS is performed on a grid consisting of $410 \times 160 \times 112$ points in the streamwise, spanwise and wall-normal directions (a total of approximately 7.3 million points). The grid points are uniformly spaced in the streamwise and spanwise directions, whereas they are

https://doi.org/10.1017/jfm.2011.560 Published online by Cambridge University Press

clustered in the wall-normal direction according to a hyperbolic sine transformation. The principal DNS is performed on a grid consisting of $1024 \times 160 \times 128$ points in the streamwise, spanwise and wall-normal directions (a total of approximately 21 million points). The grid points are uniformly spaced in the spanwise direction, whereas they are clustered in the streamwise and wall-normal directions according to a hyperbolic sine transformation. The clustering in the streamwise direction is centred at the location of the corner. Unless otherwise stated, the reference plane at which grid resolutions, inflow conditions etc. are given in this paper is the inflow plane of the principal DNS (equivalently, the recycling plane of the auxiliary DNS). At the reference plane, the grid resolution in the streamwise direction is $\Delta x^+ = 7.5$, which is also the maximum grid spacing in the streamwise direction across the domain. The '+' superscript denotes non-dimensionalization by the inner length scale ν_w/u_τ, where ν_w is the kinematic viscosity at the wall and $u_\tau = \sqrt{\tau_w/\rho_w}$ is the friction velocity (τ_w is the skin friction and ρ_w is the density at the wall). The minimum grid spacing in the streamwise direction occurs at the corner and is $\Delta x^+_{corner} = 3.5$ (where the non-dimensionalizing inner length scale is still taken at the reference plane). In the wall-normal direction at the reference plane, the first grid point above the wall is located at $\Delta z_1^+ = 0.2$. The uniform grid spacing in the spanwise direction is $\Delta y^+ = 4.3$.

2.3. *Initial and boundary conditions*

The initial flow field for the auxiliary DNS is generated according to the method of Martín (2007), whereas for the principal DNS a flow field from the previous DNS by Wu & Martín (2007) is used for initialization.

Except for the inflow, the same boundary conditions are used in the auxiliary and principal DNS. A no-slip isothermal boundary condition is specified at the wall with $T_w = 307$ K, which is approximately equal to the adiabatic wall recovery temperature. A supersonic outflow boundary condition is specified at the lid and outlet of the computational domain, and in the spanwise direction periodicity is specified. As discussed above, the inflow boundary condition for the auxiliary DNS is prescribed by means of the recycling–rescaling method of Xu & Martín (2004). At every time step in the auxiliary DNS, the flow data on four spanwise–wall normal planes surrounding the recycling plane are saved. As shown in figure 1 the saved flow data are used to prescribe the inflow boundary condition for the principal DNS. The data are required on four planes to satisfy the boundary condition requirement of the selected WENO scheme. At runtime for the principal DNS, the saved inflow data are interpolated linearly in time to the instants dictated by the time stepping in the principal DNS. In addition, the saved inflow data are linearly interpolated from the auxiliary DNS grid onto the principal DNS grid. The interpolation is only required in the streamwise (x) and wall-normal (z) directions, but not in the spanwise (y) direction in which the two grids are identical.

2.4. *Rescaling length*

The rescaling length is 7.3δ as indicated in figure 1. With the reference location fixed at the inflow of the auxiliary DNS, the autocorrelation of the u velocity as a function of streamwise separation (not shown here) decays to zero half-way through the rescaling box, and this is the criterion according to which the rescaling length is selected. This selection criterion is based on the Eulerian decorrelation distance of the eddies, and as such it only guarantees the absence of spurious correlation being introduced in the rescaling box from an Eulerian viewpoint. Spurious periodicity could

https://doi.org/10.1017/jfm.2011.560 Published online by Cambridge University Press

still be present in the flow since the Lagrangian decorrelation time of the eddies as they are being convected by the mean velocity is significantly larger, as discussed by Simens *et al.* (2009). Large-scale eddies take a significantly longer time to decorrelate with themselves as they are being convected by the mean velocity than suggested by the length scale of the autocorrelation function. For incompressible flows, Simens *et al.* (2009) argue that a large eddy of size $O(\delta)$, with internal velocity $O(u_\tau)$ and convection velocity $O(U_\infty)$, will decorrelate with itself as it convects over a distance $O(U_\infty \delta/u_\tau)$. Extending this argument to compressible flows, the eddy decorrelation length scale is $O(\sqrt{\rho_\infty} U_\infty \delta/\sqrt{\rho_w} u_\tau)$, since the appropriate velocity scale for a large eddy is $O(\sqrt{\rho_w} u_\tau/\sqrt{\rho_\infty})$ according to Morkovin's hypothesis. To eliminate spurious periodicity in the flow, the recycling plane would need to be located sufficiently far downstream from the inflow plane to accommodate the Lagrangian eddy decorrelation length, implying for the present flow conditions a rescaling length of $O(30\delta)$. Using such large rescaling lengths would be costly, and for the present simulation we choose a more moderate value, which satisfies the Eulerian decorrelation criterion but not the Lagrangian criterion. Consequently, some forcing due to the rescaling is present in the DNS, but we show in § 3.2 that this forcing has no significant effect on the properties of the low-frequency unsteadiness in the sense that, based on the temporal, spectral and statistical analysis presented in § 3.2, the properties of the low-frequency unsteadiness in the present DNS are in agreement with the previous literature.

2.5. *Free stream filtered inflow*

Under the conditions considered here, the coupling between the recycling and inflow plane appears to be mildly unstable in the free stream, where a gradual increase of the turbulence level is observed over time, whereas inside the boundary layer the turbulence intensities are stationary. These observations hold over time scales corresponding to the duration of the DNS, which is more than $1000\delta/U_\infty$. Instantaneous flow fields (not shown here) reveal that in the free stream the forcing generates acoustic disturbances, which tend to be oriented in the vertical direction, originate some distance above the boundary layer at random locations in the free stream and can extend over large distances in the wall-normal and spanwise directions, in some cases of the order of a few boundary layer thicknesses. There also appears to be a preference for acoustic waves travelling upstream with respect to the flow rather than downstream. This spurious free stream mode is mildly unstable, gradually raising, for example, the mass flux turbulence intensity $(\rho u)_{rms}/\langle \rho u \rangle$ in the free stream to $O(0.1)$ over the entire duration of the DNS of $1000\delta/U_\infty$ (here $(\cdot)_{rms}$ denotes the root mean square of the enclosed quantity, and $\langle \cdot \rangle$ denotes the mean). The quality of the simulation would be deteriorated by this spurious free stream mode, and a modification is made in the auxiliary DNS with the purpose of damping this mode. The modification consists in periodically applying a free stream filter in the auxiliary DNS. We consider this modification to be minor and non-intrusive in the sense that the filtering acts only in the free stream and has no direct effect on the actual boundary layer flow. Details of this approach, including a validation of the auxiliary DNS demonstrating the accuracy of the free stream filtering approach, may be found in Priebe & Martín (2009).

For completeness, it should be noted that a Cartesian version of the DNS code is used in the auxiliary simulation (as opposed to the full curvilinear version used in the principal simulation). In addition, the WENO limiters are switched off in the auxiliary simulation, where the symmetric bandwidth-optimized WENO scheme is used on its own. The justification for this is that simulations of boundary layers are less stringent

https://doi.org/10.1017/jfm.2011.560 Published online by Cambridge University Press

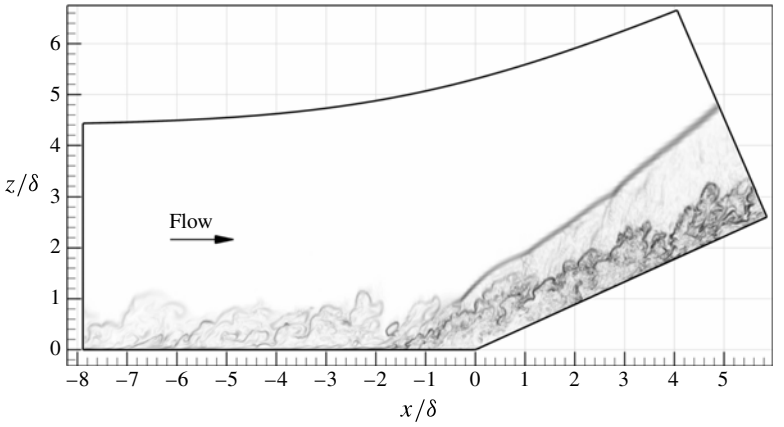


FIGURE 2. Instantaneous flow visualization on a streamwise–wall normal plane. Greyscale contour map of nonlinear transformation of magnitude of density gradient (numerical Schlieren).

M	Re_θ	δ^+	U_∞ (m s^{-1})	δ (mm)	δ^* (mm)	θ (mm)	H
2.91	2.9×10^3	3.4×10^2	610	7.1	2.58	0.47	5.49

TABLE 1. Characteristics of the incoming boundary layer.

and may accurately be performed with the symmetric bandwidth-optimized WENO scheme without the limiters.

3. Results

3.1. *Instantaneous and mean flow organization*

The main parameters of the incoming boundary layer, which is fully turbulent, are listed in table 1, where the thickness δ is based on 99 % of the free stream velocity U_∞, δ^* is the displacement thickness (compressible definition), θ is the momentum thickness (compressible definition), and H is the shape factor. The Reynolds number is defined as $Re_\theta = U_\infty \theta / \nu_\infty$, where ν_∞ is the kinematic viscosity in the free stream, and the Kármán number is defined as $\delta^+ = \delta u_\tau / \nu_w$, where u_τ is the friction velocity and ν_w is the kinematic viscosity at the wall. The geometry for the interaction is a compression ramp with ramp angle $\phi = 24°$. A numerical Schlieren of the interaction is shown in figure 2, and a three-dimensional visualization is shown in figure 3.

The separation length is determined from the mean C_f distribution (figure 4*a*) and is $L_{sep}/\delta = 3.0$. The location of the separation point is $x_s^*/\delta = -2.1$, and the location of the reattachment point is $x_r^*/\delta = 0.9$, where the coordinate x^* is measured along the wall with the origin being located at the corner. The separation is not uniformly strong in the sense that the skin friction coefficient varies with streamwise distance inside the separated flow region. The C_f distribution has five local extrema inside the separated flow region: there is a local minimum a short distance downstream of separation at approximately $x^*/\delta = -1.7$; this is followed by an increase of C_f towards

https://doi.org/10.1017/jfm.2011.560 Published online by Cambridge University Press

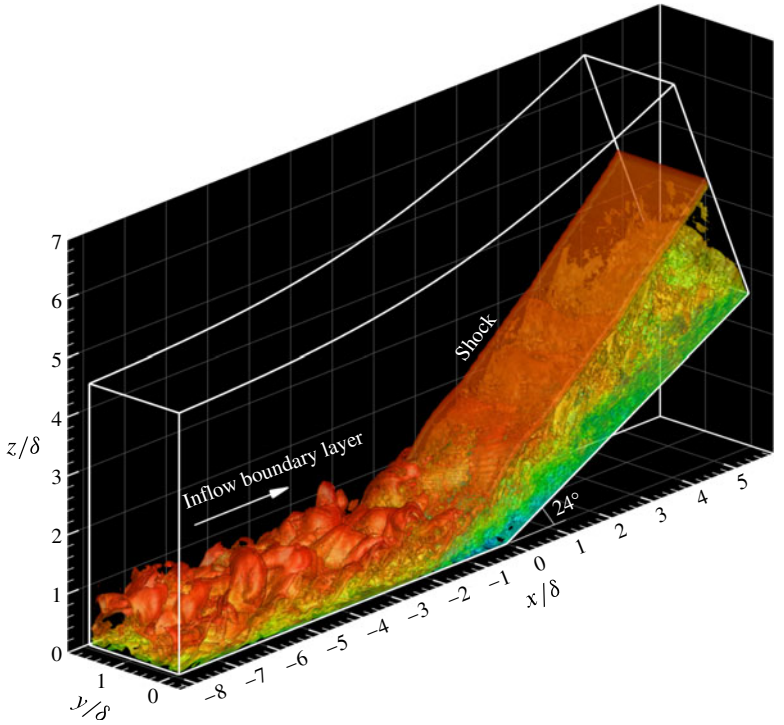


FIGURE 3. Instantaneous flow visualization. Isosurface of magnitude of density gradient, $|\nabla\rho|\delta/\rho_\infty = 2.5$, coloured by the streamwise velocity component (with levels from $-0.4U_\infty$ to U_∞, blue to red).

a local maximum at approximately $x^*/\delta = -1.0$; three local extrema are present near the corner, with a local minimum just upstream of the corner, followed by a local maximum at the corner, and another local minimum just downstream of the corner. The maximum at the corner is probably due to the fact that the wall-normal direction changes discontinuously there, whereas the flow direction changes smoothly, which could explain the observed reduction in the magnitude of C_f in the neighbourhood of the corner. According to this argument, the maximum at the corner is of little physical interest and may be ignored in the C_f distribution in figure 4(*a*), leaving effectively three local extrema inside the separated flow region. As will be shown later, this structure of the mean C_f distribution inside the separated flow region appears to be related to the low-frequency unsteadiness. The mean flow is less strongly separated in a region surrounding $x^*/\delta = -1$, and this appears to be related to collapses of the separation bubble and the changes of flow topology that occur during the low-frequency unsteadiness; this will be discussed in detail in §§ 3.4 and 4. The wall pressure distribution (figure 4*b*) has three inflection points and shows the development of a pressure plateau in the separated flow region as is typical for STBLI flows with mean flow separation.

The flow is composed of five flow regions, which are indicated on the time- and spanwise-averaged flow field in figure 5 by the letters A–E: the incoming turbulent boundary layer (A); the shock (B), which is shown in the figure by an isocontour of pressure gradient $|\nabla p|\delta/p_\infty = 2$; the separated shear layer (C), which is shown by a contour map of the spanwise vorticity ω_y; the recirculation bubble in the corner

https://doi.org/10.1017/jfm.2011.560 Published online by Cambridge University Press

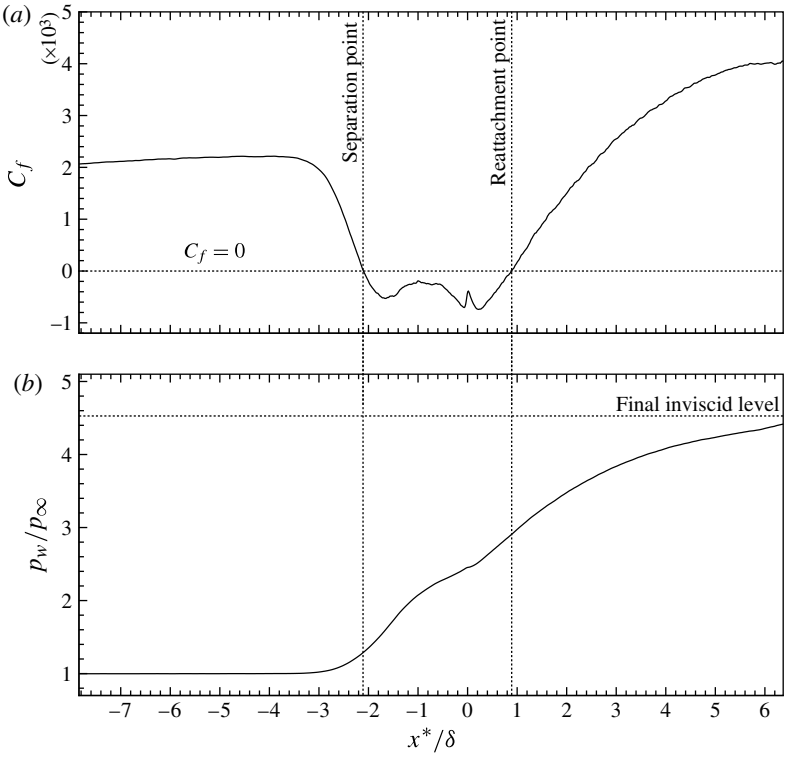


FIGURE 4. Time- and spanwise-averaged distribution of: (*a*) skin friction coefficient C_f; and (*b*) wall pressure.

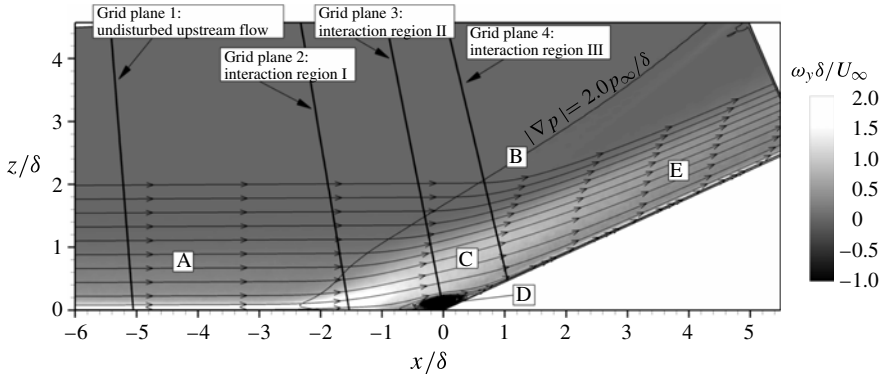


FIGURE 5. Mean flow organization. See text for details. The grid planes are referenced in § 3.2.

(D), which is shown in the figure by (u, w) streamlines; and the downstream out-of-equilibrium boundary layer (E).

To describe in more detail the mean flow in the shear layer (C), profiles of streamwise velocity u and of spanwise vorticity ω_y are plotted in figure 6 at several streamwise locations starting at $x/\delta = -3$ (upstream of separation) and up to the corner. Generally speaking, the velocity profiles in the shear layer resemble those of a

https://doi.org/10.1017/jfm.2011.560 Published online by Cambridge University Press

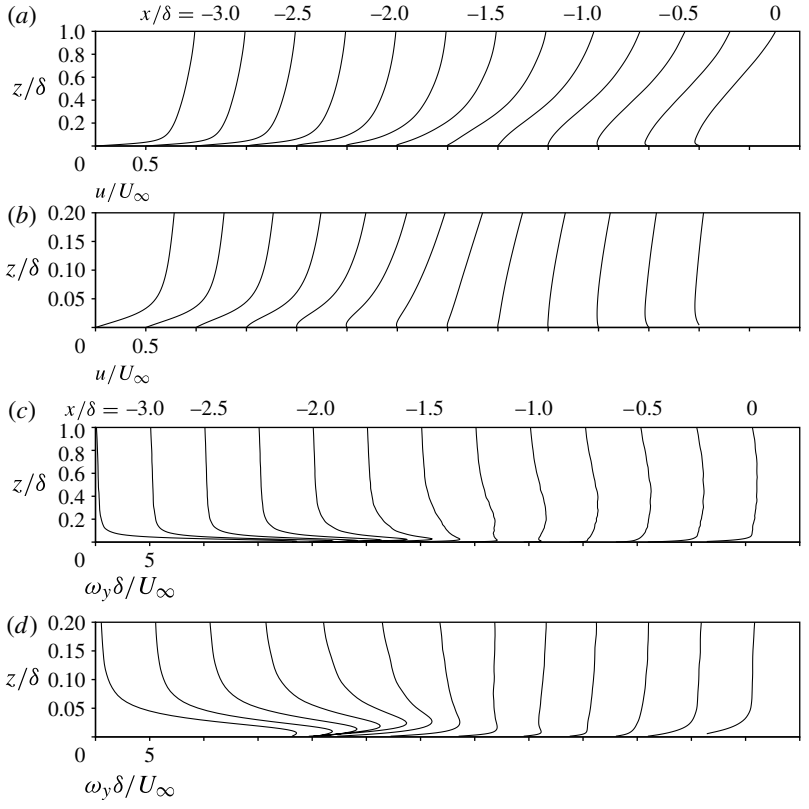


FIGURE 6. Mean profiles: (*a*) streamwise velocity; (*b*) detail of streamwise velocity near wall; (*c*) spanwise vorticity; and (*d*) detail of spanwise vorticity near wall.

plane mixing layer: the low-speed side (reversed flow near the wall) is connected to the high-speed side (free stream) through profiles that have a single inflection point, located roughly in the middle of the layer. Consistent with this observation on the velocity profiles, the vorticity profiles show a maximum roughly in the middle of the layer. These observations about the shear layer profiles in a compression ramp flow agree with previous experimental observations for the reflected shock configuration (Dupont *et al.* 2008; Souverein *et al.* 2010), where it has also been shown that the shear layer profiles resemble those of a mixing layer.

The statement that the profiles downstream of separation are mixing-layer-like in the present DNS must be qualified somewhat in view of the behaviour of some of the profiles close to the wall ($z/\delta < 0.1$): there are some departures from mixing-layer-like profiles with a single inflection point at $x/\delta = -1.25$ and $x/\delta = -1$, where a second maximum of vorticity is observed close to the wall. Further away from the wall, these profiles are still mixing-layer-like, showing a maximum of vorticity in the middle of the separated shear layer and an associated inflection point in the velocity profiles. In addition to having a second maximum of vorticity close to the wall, the profiles at $x/\delta = -1.25$ and $x/\delta = -1$ also show that the magnitude of vorticity at the wall is significantly smaller in this region than nearer to separation or the corner. In fact, from figure 6(*d*) it is apparent that the magnitude of vorticity at the wall has a maximum downstream of separation, followed by a decrease towards a minimum

https://doi.org/10.1017/jfm.2011.560 Published online by Cambridge University Press

around $x/\delta = -1$ and subsequently an increase towards the corner. This behaviour is consistent with the variation of C_f inside the separated flow region as shown in figure 4(*a*) and discussed above.

In § 3.4, it will be shown that a low-frequency mode exists in the flow. The shock, the shear layer and the recirculation bubble participate in this low-frequency mode, which involves significant departures from the mean flow shown in figures 5 and 6. During the phase of the low-frequency mode when the shock moves downstream, large peaks of vorticity are observed close to the wall in a streamwise interval extending from somewhere downstream of separation to somewhere upstream of the corner, and the flow may reattach in that interval. This will be discussed in detail in § 3.4; the reason for briefly mentioning these observations here is that the vorticity peaks observed in the mean flow close to the wall at the streamwise locations $x/\delta = -1.25$ and $x/\delta = -1$ may be interpreted as the imprint on the mean flow of the phase of the low-frequency mode when the shock moves downstream.

The term 'phase' has one of two meanings in the present paper, depending on the context. It may be used according to the usual definition to refer to the phase angle between two (Fourier-analysed) signals. Alternatively, it may refer to different 'stages' of the low-frequency motion, where these stages are defined based on an indicator of the motion such as the recirculation bubble size and growth rate or the shock position and velocity. For example, if one were to take the properties of the recirculation bubble as an indicator of the motion, one may identify 'phases' of the motion associated with large, small and intermediate-size (growing or collapsing) bubbles.

Since the shear layer velocity profiles shown in figure 6 contain an inflection point, they are inviscidly unstable. The shear layer rolls up and vortical structures are formed typical of a Kelvin–Helmholtz type of instability. The vortical structures in the shear layer are visualized in figures 7 and 8, which show four instantaneous uncorrelated DNS flow fields; in the figures, the reversed flow region in the corner is made visible by the isosurface of streamwise velocity $u = 0$; and the vortical structures are made visible by an isosurface of the swirling strength. Concerning the structure of the reversed flow region, it is apparent from the figures that the separation line is relatively uniform across the span, whereas the reattachment line shows significant spanwise variation. At reattachment, alternating streamwise-oriented stripes of reversed and attached flow are observed in many of the instantaneous realizations – see figure 7(*b*) and figure 8(*a*). Few vortical structures are visible in the incoming boundary layer given the relatively high threshold of the swirling strength used in the visualizations – see figure 8(*a*). At separation, spanwise-oriented vortices with strong positive spanwise vorticity are formed. The vortices are three-dimensional, and from visual inspection of figures 7 and 8 their spanwise scale is probably of order 0.2δ. In addition to the spanwise-oriented vortices, some streamwise-oriented vortices are also visible downstream of separation. In general, strong vortical structures populate the shear layer above the reversed flow region from separation to reattachment, and vortical structures are also visible past reattachment in the downstream flow.

A characteristic of separated shear layer flows is the formation of large-scale vortices through a vortex growth and pairing process as the shear layer develops. The presence of large-scale vortices has been shown in incompressible separated shear layers (see e.g. Cherry, Hillier & Latour 1984; Na & Moin 1998). PIV measurements in the reflected shock interaction have also shown the presence of large-scale vortices, both in incipiently separated cases (Humble, Scarano & van Oudheusden 2009*b*; Souverein *et al.* 2010) and in fully separated cases (Dupont *et al.* 2008; Souverein

https://doi.org/10.1017/jfm.2011.560 Published online by Cambridge University Press

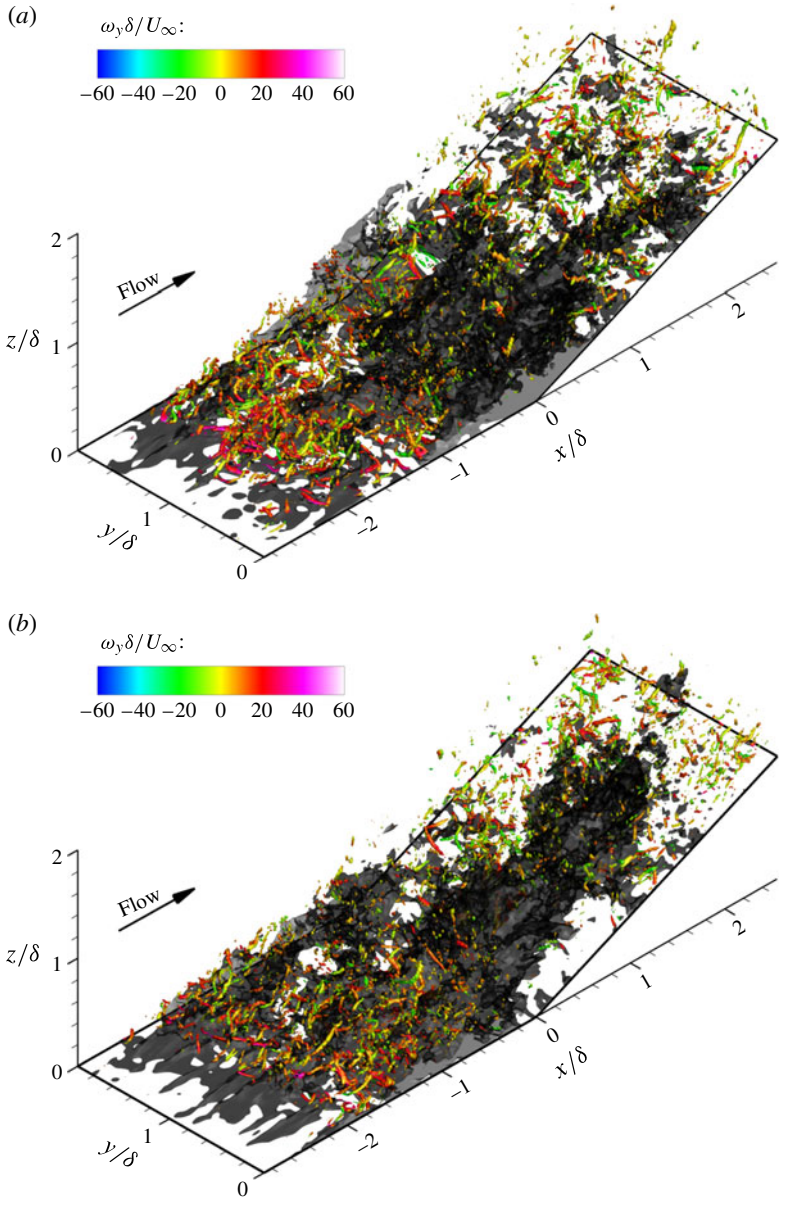


FIGURE 7. Instantaneous structure of the reversed flow and the shear layer vortices. Isosurface of streamwise velocity $u = 0$ (in black), and isosurface of swirling strength $\lambda_{ci} = 40\langle\lambda_{ci}\rangle$ (coloured by the spanwise vorticity), where $\langle\lambda_{ci}\rangle$ is the time- and space-averaged swirling strength. These two typical flow fields are uncorrelated.

et al. 2010). Concerning the present DNS, the visualizations in figures 7 and 8 probably do not bring out the large-scale vortices particularly clearly – smaller-scale features are predominant in these visualizations – although the cores of the large-scale vortices are probably visible. In any case, the presence of large-scale vortices in the DNS will be shown spectrally in § 3.2.

https://doi.org/10.1017/jfm.2011.560 Published online by Cambridge University Press

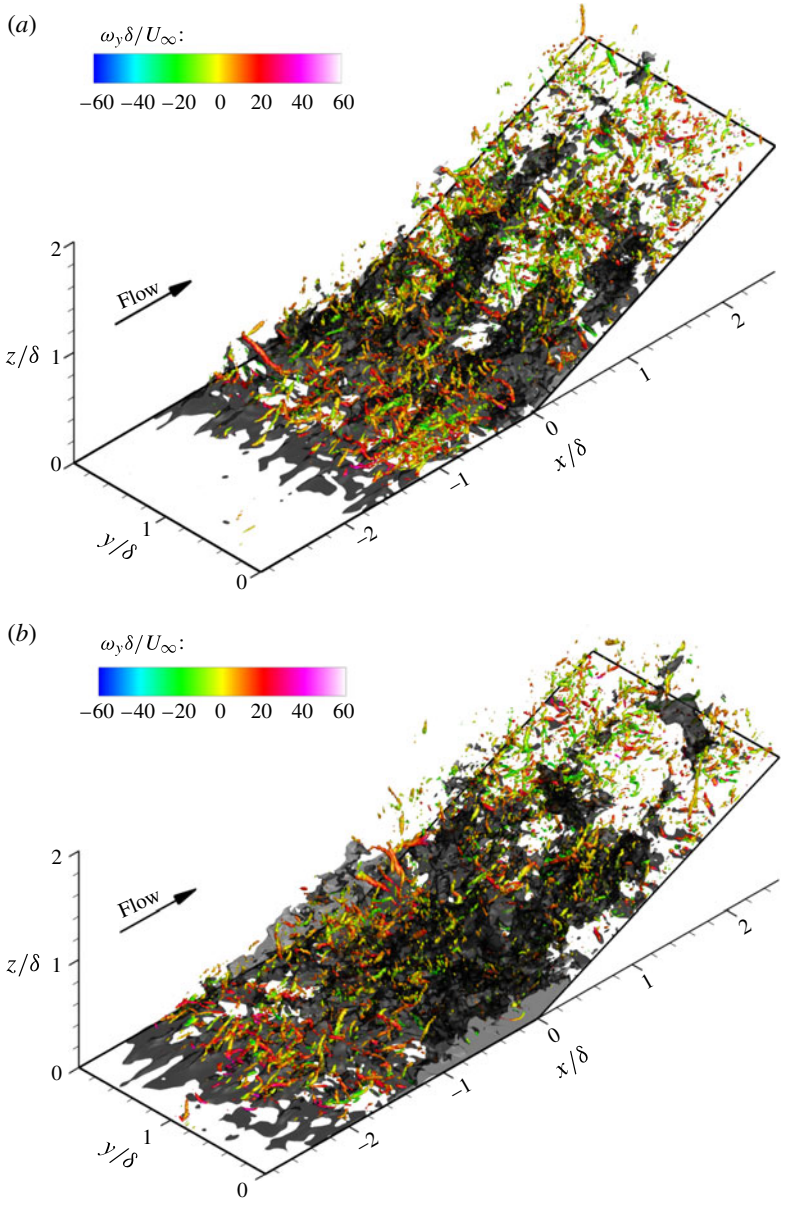


FIGURE 8. Same as figure 7. These other two typical flow fields are also uncorrelated.

3.2. *Low-frequency unsteadiness: spectral and statistical analysis*

Several time signals from the DNS are shown in figures 9–11 in order to illustrate the unsteadiness in the flow. Concerning figure 9, the location of the spanwise-averaged separation point $x_s(t)$ is obtained as follows: at each time step during the DNS, the spanwise-averaged flow field is traversed along the streamwise direction starting from the inlet of the computational domain; the first point that satisfies the condition $C_f \leqslant 0$ is retained and identified with the instantaneous value of x_s. The location of the spanwise-averaged reattachment point $x_r(t)$, shown in figures 9 and 10, is obtained

https://doi.org/10.1017/jfm.2011.560 Published online by Cambridge University Press

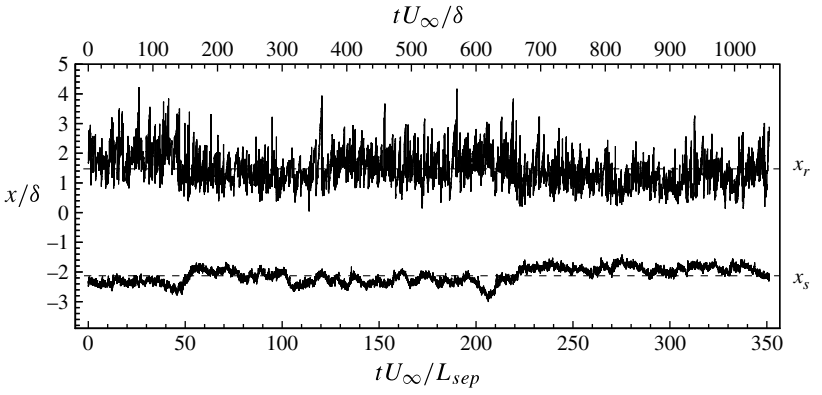


FIGURE 9. Location of spanwise-averaged separation point x_s and reattachment point x_r. The mean values are indicated by the dashed lines.

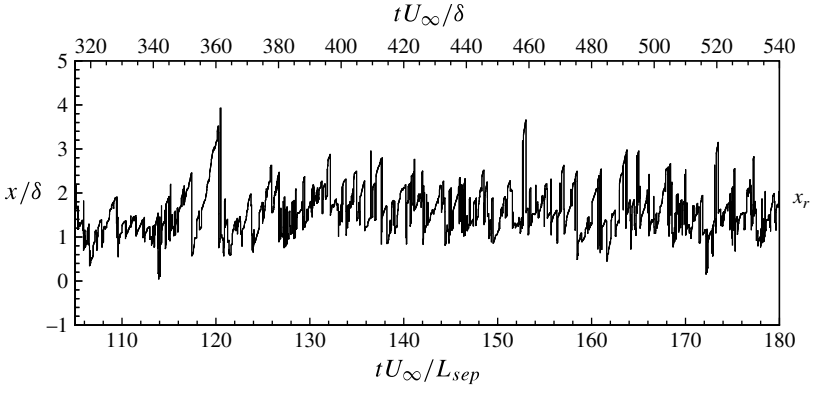


FIGURE 10. Detail of figure 9 showing the location of the spanwise-averaged reattachment point on a shorter time scale.

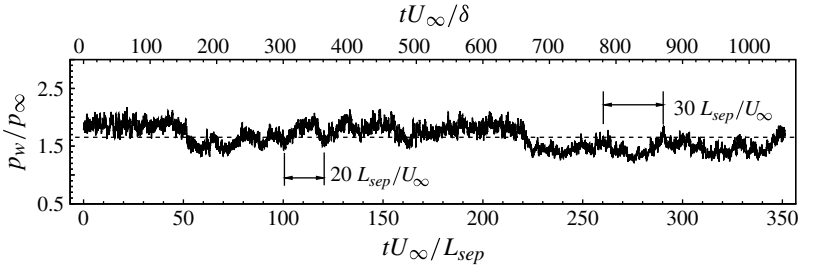


FIGURE 11. Spanwise-averaged wall pressure signal in the interaction region ($x/\delta = -1.53$).

in a similar manner: the spanwise-averaged flow field is traversed along the negative streamwise direction starting from the outlet of the computational domain, and the first point that satisfies the condition $C_f \leqslant 0$ is identified with the instantaneous value of x_r.

The low-frequency unsteadiness is apparent in the motion of the separation point (figure 9) and in the variation of the wall pressure in the interaction region

https://doi.org/10.1017/jfm.2011.560 Published online by Cambridge University Press

(figure 11). Consistent with experimental observations, the low-frequency unsteadiness is irregular and aperiodic; it is a broadband motion involving a range of time scales. Dussauge *et al.* (2006) found that the central frequency of the unsteadiness scales relatively well on U_∞/L_{sep}. For several flow geometries and over a range of Reynolds and Mach numbers, the unsteadiness occurs at frequencies centred about $St = f\,L_{sep}/U_\infty = 0.02$–$0.05$ (i.e. time scales $tU_\infty/L_{sep} = 20$–50). Two motions in this range of time scales, one at $tU_\infty/L_{sep} = 20$ and the other at $tU_\infty/L_{sep} = 30$, are highlighted in the wall pressure signal in figure 11. In addition, motions over shorter and longer time scales than the principal one are apparent in figures 9 and 11, illustrating the broadband character of the low-frequency unsteadiness. During the time range $120 \leqslant tU_\infty/L_{sep} \leqslant 190$, for example, a succession of upstream–downstream motions on a relatively shorter time scale of approximately $tU_\infty/L_{sep} = 10$ is visible in figure 9. The data also show a modulation of the low-frequency unsteadiness on a time scale that is almost an order greater than the principal time scale: the wall pressure signal in figure 11 is modulated on a time scale that is probably comparable to about half the duration of the DNS data set. The DNS thus contains a broadband unsteadiness that involves a wide range of low frequencies comparable to those seen in experiments (see Dussauge *et al.* 2006). This unsteadiness will be characterized in more detail below using spectral analysis.

The reattachment point in figure 9 shows some low-frequency fluctuations, which appear to be out of phase with the separation point fluctuations, i.e. when the separation point moves upstream (away from the corner), the reattachment point moves downstream (also away from the corner), and vice versa. At the wall, the separated flow region thus appears to undergo a low-frequency breathing motion with repeated growth and shrinking of the extent of separation. However, these low-frequency motions do not seem to be the dominant contribution to the fluctuations of x_r. An unsteadiness at higher frequencies, which is apparent in figure 10, appears to be energetically dominant. The reattachment point follows a sawtooth-like trajectory: it moves downstream at almost constant speed, followed by a rapid relaxation in the upstream direction. A particularly clear example of such a sawtooth motion occurs around $tU_\infty/L_{sep} = 120$ (see figure 10). The period of this particular sawtooth motion is approximately $tU_\infty/L_{sep} = 2.5$, and the amplitude is approximately 3.5δ. In general, the sawtooth motions appear to have a period $O(L_{sep}/U_\infty)$ and an amplitude $O(\delta)$. Sawtooth-like motions of the reattachment point are also known to exist in incompressible separated shear layers, and they are attributed to the passage near reattachment of large-scale vortical structures formed in the shear layer and shed into the downstream flow (Kiya & Sasaki 1983, 1985; Na & Moin 1998; Lee & Sung 2002).

In order to analyse in more detail which scales are present in the flow, power spectra are presented in what follows. Welch's method is used for spectral estimation with eight segments and 50 % overlap. A Hamming window is used for weighting the data on each segment prior to fast Fourier transform (FFT) processing. Using the above segmentation parameters, the length of an individual segment is approximately $233\delta/U_\infty$ ($78L_{sep}/U_\infty$), and time scales longer than this are thus not resolved in the spectra shown. The sampling frequency of the data is approximately $f_s = 200U_\infty/\delta$.

Figure 12 shows that the separation point has most of its energy at low frequencies, and these frequencies are consistent with the range of frequencies found in experiments (see Dussauge *et al.* 2006). The reattachment point has some energy at these low frequencies, but most of the energy is contained at higher frequencies centred about approximately $St = 0.5$, and this energy is associated with the passage

https://doi.org/10.1017/jfm.2011.560 Published online by Cambridge University Press

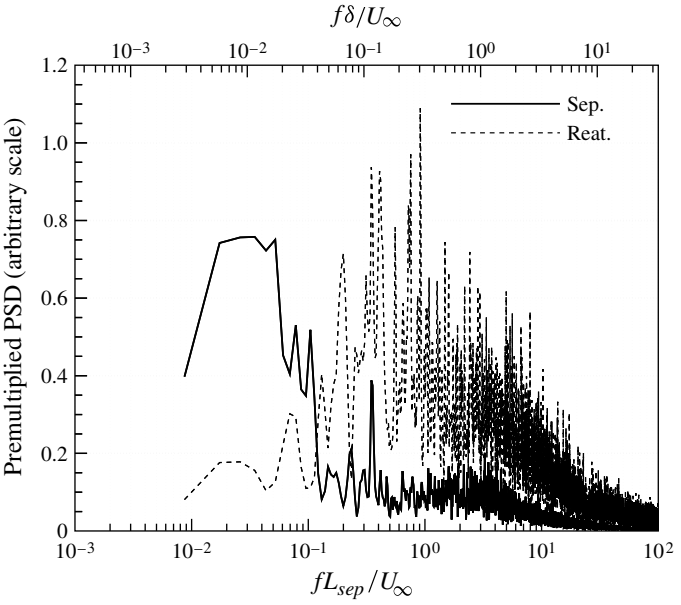


FIGURE 12. Power spectra of spanwise-averaged separation and reattachment location.

near reattachment of large-scale vortical structures that are formed in the shear layer and subsequently shed into the downstream flow. This behaviour is also seen in incompressible separated shear layers. The characteristic frequency associated with the shedding of large-scale vortices was found to be $St = f L_{sep}/U_\infty = 0.65$ in the closed separation bubble formed at the leading edge of a blunt flat plate with right-angled corners by Kiya & Sasaki (1983, 1985), $St = 0.48$ in backward-facing step flow by Lee & Sung (2002), and roughly in the range $St = 0.25$–1 in the DNS by Na & Moin (1998) of a closed separation bubble on a flat plate induced by an adverse-to-favourable pressure gradient. These characteristic frequencies found in incompressible separated shear layers are in general agreement with the value found here.

The low-frequency unsteadiness is also apparent from spectra of the wall pressure. Figure 13(*a*) shows the spectrum of the wall pressure in the undisturbed incoming boundary layer. The spectrum consists of a broadband bump centred about $f\delta/U_\infty = 1$, which is the characteristic frequency of the energetic scales in the incoming boundary layer. Superimposed on this broadband turbulence bump, there are three narrowband peaks associated with the rescaling method used for generating the turbulent inflow. The peaks are located at the rescaling fundamental frequency, and at its second and third harmonics. No significant energy is present in the incoming boundary layer at frequencies $St \leqslant 0.1$, that is, in the range of frequencies associated with the low-frequency shock motion. Near the separation shock foot (figure 13*b*,*c*), the wall pressure spectra show, in addition to the broadband bump associated with the turbulence, a second broadband bump at much lower frequencies between $St = 0.01$ and 0.1, and this is due to the low-frequency shock motion. Near reattachment (figure 13*d*), some energy is still present at the low frequencies, but most of the energy is contained at higher frequencies associated with the turbulent scales. Comparing the spectrum in the incoming boundary layer (figure 13*a*) with that near reattachment (figure 13*d*), it is apparent that the central frequency of the turbulent scales shifts

https://doi.org/10.1017/jfm.2011.560 Published online by Cambridge University Press

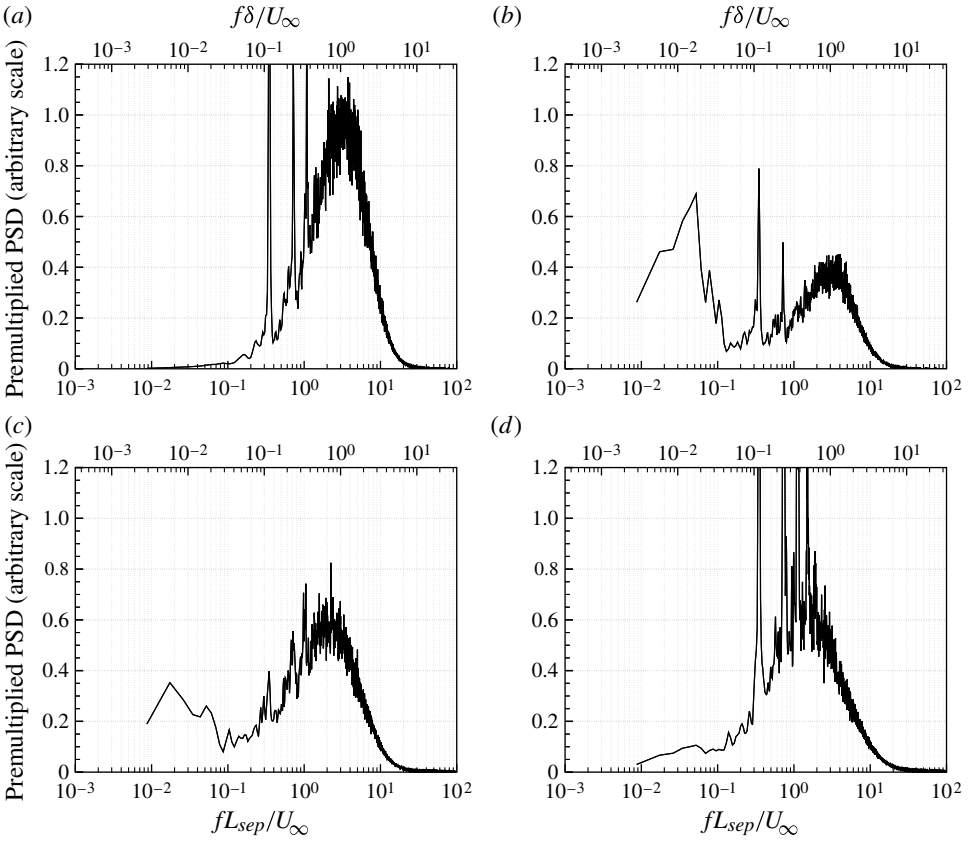


FIGURE 13. Power spectra of wall pressure at different streamwise locations: (*a*) $x/\delta = -5.05$; (*b*) $x/\delta = -2.48$; (*c*) $x/\delta = -1.53$; and (*d*) $x/\delta = 1.05$.

to slightly lower values through the interaction, from $f\delta/U_\infty = 1$ in the incoming boundary layer to approximately $f\delta/U_\infty = 0.5$ near reattachment.

In addition to the four individual spectra shown in figure 13, the full evolution of the wall pressure spectrum through the interaction is shown in figure 14. The dominant scale shifts from turbulent frequencies in the incoming boundary layer to low frequencies associated with the shock motion in the region surrounding separation and back to turbulent frequencies in the downstream flow. This behaviour of the wall pressure fluctuations agrees with experimental findings for the compression ramp interaction (see, among many other references, Ringuette *et al.* 2009) and the reflected shock interaction (e.g. Dupont *et al.* 2006).

In the remainder of this section, the statistical link between the low-frequency shock motion and various signals at the wall and in the flow field is investigated by means of the statistical quantities of coherence and phase. The coherence $\gamma_{xy}^2(f)$ between two time signals $x(t)$ and $y(t)$ is a real-valued quantity defined as

$$\gamma_{xy}^2(f) = \frac{|P_{xy}(f)|^2}{P_{xx}(f)P_{yy}(f)}, \tag{3.1}$$

where $P_{xx}(f)$ denotes the power spectral density of signal $x(t)$, and $P_{xy}(f)$ denotes the cross-power spectral density between signals $x(t)$ and $y(t)$. For all f, the coherence

https://doi.org/10.1017/jfm.2011.560 Published online by Cambridge University Press

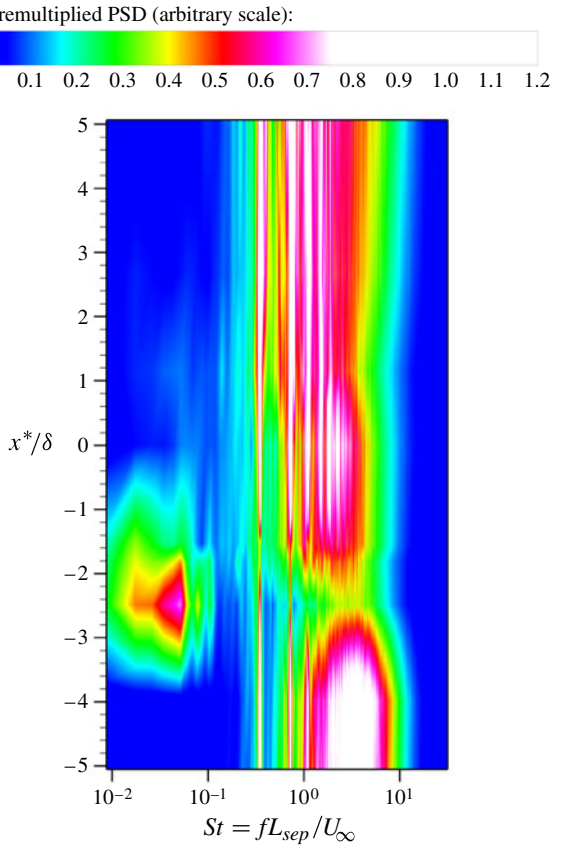


FIGURE 14. Contour map of wall pressure power spectrum.

satisfies

$$0 \leqslant \gamma_{xy}^2(f) \leqslant 1. \tag{3.2}$$

If $\gamma_{xy}^2(f) = 1$, the time signals $x(t)$ and $y(t)$ are linearly related at frequency f in the sense of the convolution filter; if $\gamma_{xy}^2(f) = 0$, they are unrelated. The coherence may be viewed as 'analogous to the square of the correlation coefficient (with time lag)' (Bendat & Piersol 2000, p. 197).

One of the two time signals based on which the coherences and phases in this section are calculated is a reference signal that indicates the shock motion in the free stream. This signal is referred to as the shock indicator signal, and it is the pressure signal obtained at $z/\delta = 1.4$ on grid plane 3 (see figure 5). The location of the second signal is variable.

The coherence and phase between the shock indicator signal and the location of separation and reattachment is shown in figure 15. Concerning the location of separation, high values of coherence are observed at low frequency; the shock indicator signal and the separation signal are almost linearly related. In addition, the two signals are approximately out of phase, so that, when the shock indicator signal rises because the shock moves upstream across the measurement location, the separation signal falls because the separation point moves upstream (away from the corner), and vice versa. The shock in the free stream and the separation point at the

https://doi.org/10.1017/jfm.2011.560 Published online by Cambridge University Press

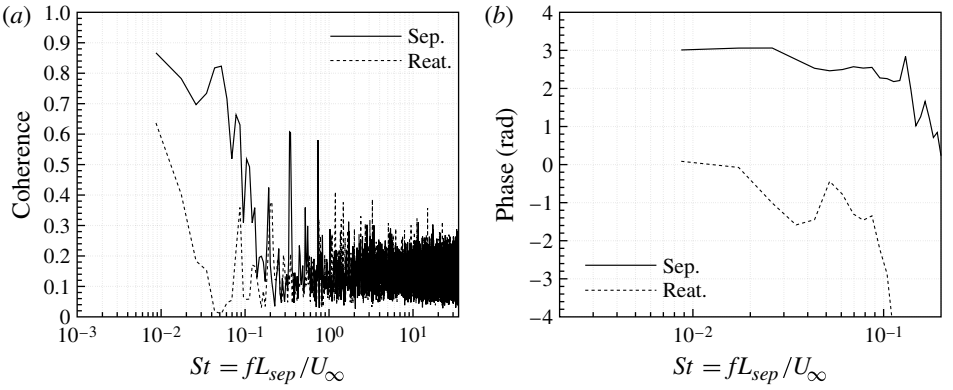


FIGURE 15. Statistical link between the shock indicator signal and the spanwise-averaged separation and reattachment location, respectively: (*a*) coherence and (*b*) phase.

wall thus move almost synchronously in the upstream–downstream direction at low frequency. In addition to the high values of coherence observed at low frequency, two narrowband peaks are also observed at the rescaling frequency and its second harmonic.

Concerning the location of reattachment, high values of coherence are observed at the lowest resolved frequencies, and the signals are in phase at these frequencies, which implies that, when the shock in the free stream moves upstream, the reattachment point moves downstream (away from the corner). It should be noted, however, that the reattachment coherence rises to large values only at much lower frequencies than the separation coherence. At $St = 0.05$, for example, which is in the range of frequencies associated with the shock unsteadiness, the separation coherence has a value of approximately 0.8, indicating an almost linear relationship, whereas the reattachment coherence is essentially zero. It is not clear what causes the absence of reattachment coherence at these frequencies since it will be shown next that wall pressure fluctuations near reattachment show a definite coherence with the shock indicator signal, so that low-frequency motions near reattachment and motions of the shock are statistically linked in the DNS.

Figure 16 shows the coherence between the shock indicator signal and the wall pressure at different streamwise locations. The low-frequency shock motion in the free stream is almost linearly related to wall pressure fluctuations in the region surrounding separation, where values of the coherence as large as 0.7–0.9 are obtained for frequencies in the range $St \leqslant 0.1$ (figure 16*b*). Significant values of low-frequency coherence of around 0.5 are also observed between the shock indicator signal and wall pressure fluctuations near reattachment (figure 16*d*), showing that the low-frequency shock motion in the free stream and fluctuations near reattachment are significantly related. In the downstream flow past reattachment, the low-frequency coherence appears to decay with increasing streamwise coordinate (figure 16*d*). At the most downstream location shown, some coherence is still present. At the corner (figure 16*c*), the behaviour of the coherence at low frequency is different from all other locations shown near, or downstream of, separation in the sense that the coherence shows a peak rather than rising to a plateau. The peak occurs at a frequency of approximately $St = 0.05$ and the peak value of coherence is approximately 0.6. It is not clear what causes this 'frequency-selective' behaviour at the corner, or whether it is significant for

https://doi.org/10.1017/jfm.2011.560 Published online by Cambridge University Press

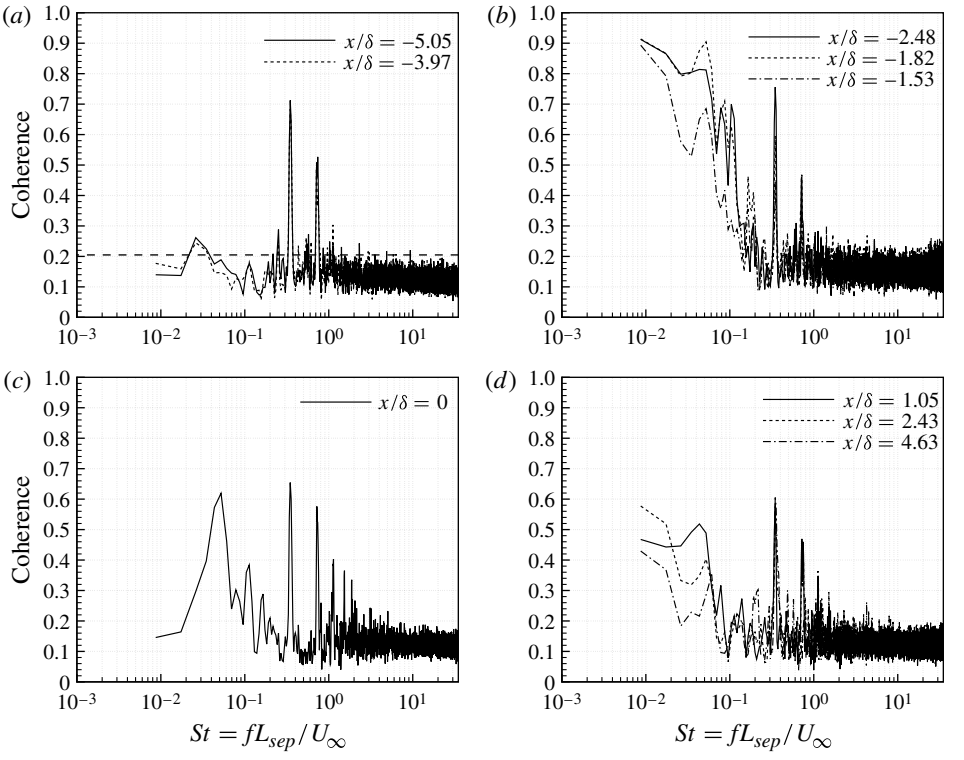


FIGURE 16. Coherence between the shock indicator signal and the wall pressure signal at different streamwise locations: (*a*) $x/\delta = -5.05$ and $x/\delta = -3.97$ (the horizontal dashed line is the 99.9 % significance limit of the coherence estimate – see text for details); (*b*) $x/\delta = -2.48$, $x/\delta = -1.82$ and $x/\delta = -1.53$; (*c*) $x/\delta = 0$; and (*d*) $x/\delta = 1.05$, $x/\delta = 2.43$ and $x/\delta = 4.63$.

the unsteadiness mechanism, but it may be expected that the presence of the corner and the constraint it imposes on the flow may locally, in the vicinity of the corner, cause some behaviour not seen elsewhere in the separation bubble. This behaviour could thus also be specific to the compression ramp geometry and not occur in other geometries such as the reflected shock case.

Figure 16(*a*) shows the coherence between the shock indicator signal and the wall pressure fluctuations in the incoming boundary layer. Two narrowband peaks associated with the rescaling are present. They are located at the rescaling fundamental frequency and its second harmonic, and this indicates that the rescaling forces the shock motion in the free stream at these two narrowband frequencies. In order to assess with confidence whether the incoming boundary layer forces the shock at any other frequencies, the 99.9 % significance limit of the coherence estimate has been determined, and this is indicated on the figure by a horizontal dashed line. The significance limit is required since the estimate of coherence is biased and noisy (see Bendat & Piersol 2000, p. 333). For any frequency f, if the *estimated* coherence lies above the 99.9 % significance limit shown, the probability that the *true* coherence equals zero is 0.1 %; or, conversely, the probability that the true coherence is strictly greater than zero in that case is 99.9 %. The significance limit was determined by means of Monte Carlo simulation. This approach has previously been used to

https://doi.org/10.1017/jfm.2011.560 Published online by Cambridge University Press

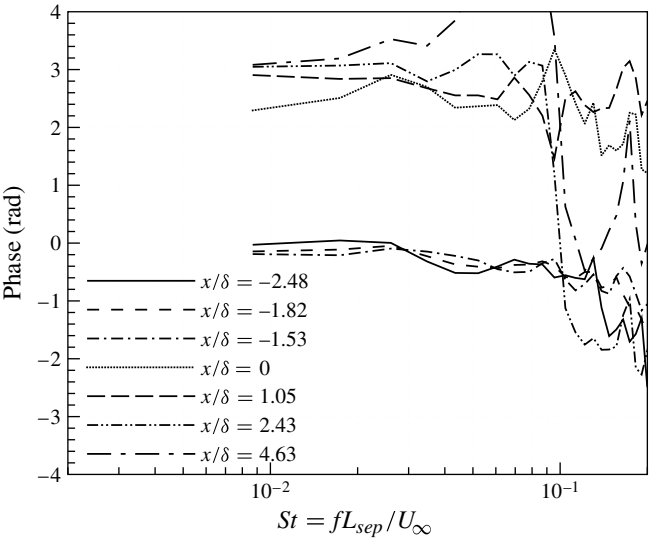


FIGURE 17. Phase between the shock indicator signal and the wall pressure signal at different streamwise locations.

determine statistical properties of coherence estimators (see e.g. Benignus 1969; Bortel & Sovka 2007). The numerical results presented in these previous works cannot be used in the present work, since the details of the coherence estimation are different.

The Monte Carlo procedure is as follows. A large number of white noise input sequences is generated. White noise sequences may be used as input without loss of generality since coherence functions are preserved under linear transformations (see Bendat & Piersol 2000, p. 200; Bortel & Sovka 2007). The generated white noise sequences are uncorrelated, i.e. the true coherence between any two sequences is zero. The sequences are processed in pairs using the same coherence estimator as was used for the actual DNS data, i.e. Welch's method with eight segments, 50 % overlap and Hamming window weighting. The process is repeated until the statistical distribution of the output (the coherence estimate) is converged. The significance limit is determined as the 99.9th percentile of the output distribution.

Returning to figure 16(*a*), except for the two rescaling peaks, which have already been discussed, there are only a few (possibly random) crossings of the significance limit. Concerning the range of low frequencies of the shock motion, there is a small-amplitude crossing around a frequency of $St = 0.03$ and this could possibly indicate a weak relation between the shock motion and the incoming boundary layer at this frequency. The crossing is of small amplitude, which implies that it could conceivably be random, and if it is not, the underlying relation is weak.

The phase at low frequency between the shock indicator signal and the wall pressure fluctuations is shown in figure 17. The signals are approximately in phase in the region surrounding separation; a phase jump of π occurs somewhere downstream of the separation region and upstream of the corner; and at the corner, near reattachment as well as downstream of it, the signals are approximately out of phase, with the phase shift appearing to increase gradually with increasing streamwise coordinate.

Summarizing the findings from figures 16 and 17, the low-frequency motion of the shock in the free stream is statistically related to the wall pressure fluctuations in the downstream separated flow region. Moreover, a phase jump of π is present somewhere

https://doi.org/10.1017/jfm.2011.560 Published online by Cambridge University Press

upstream of the corner, so that near separation the pressure fluctuations are in phase with the shock motion, whereas in the downstream part of the separated flow region, they are out of phase. These findings are consistent with experimental findings for the reflected shock case (see Dupont *et al.* 2006; Debiève & Dupont 2009). The phase jump of π in the wall pressure has also been observed in the reflected shock LES by Touber & Sandham (2009). It thus appears that, based on wall pressure fluctuations, the low-frequency unsteadiness is similar in the compression ramp and reflected shock configurations, at least in the particular flows considered. The only difference between the two configurations is probably the frequency-selective behaviour of the coherence at the corner in the compression ramp (see figure 16*c*). To the authors' knowledge no such behaviour has been reported in the reflected shock case, and this behaviour is possibly due to the particular constraint that the compression ramp geometry imposes on the flow right at the corner.

The statistical analysis is now extended away from the wall and into the flow field. Figure 18 shows the coherence between the shock indicator signal and the mass flux signal at four different locations in the flow. For regions where strong coherence is observed, the phase is given in figure 19. At the three locations shown in the flow downstream of separation (grid planes 2, 3 and 4), the low-frequency coherence has the same general structure consisting of two peaks, an inner peak and an outer peak; see figure 18(*b–d*). Note that figure 18(*c*) is truncated and the outer peak is not shown. The shock indicator signal is obtained at grid plane 3 in the free stream so that high levels of coherence are trivially present across all scales in this region, which is therefore not shown in figure 18(*c*); only the inner region of large coherence is shown. The outer peak of coherence in figure 18(*b*,*d*) is located in the shock motion region. The mass flux fluctuations in this region are approximately in phase with the shock indicator signal (see figure 19), which implies that the low-frequency shock motions are relatively uniform along the tangential direction of the shock at least over the length scales that are considered here. The inner peak of coherence is located in the separated shear layer. The mass flux fluctuations in this region are approximately out of phase with the shock indicator signal (see figure 19), which implies that, when the shock in the free stream moves upstream (i.e. when the shock indicator signal rises), the mass flux in the separated shear layer decreases, and vice versa. The shear layer thus flaps at low frequency and this flapping is related to upstream–downstream movements of the shock. In figure 18(*b–d*), the coherence generally decays as the wall is approached from the location of the inner peak. The level of coherence in the recirculation bubble near the wall is not particularly high. It will be shown in § 3.4, based on the evolution of the low-pass filtered flow field, that a definite relation between the shock and this region exists; the relation between the shock motion in the free stream and the downstream separated flow is not limited to the outer shear layer, as suggested by the coherence plots in figure 18(*b–d*), but also involves pulsations of the recirculation bubble nearer to the wall. It is possibly the nonlinearity of the relation that explains why it is not clearly apparent from the coherence in figure 18(*b–d*). The coherence between the shock indicator signal and the mass flux fluctuations in the incoming boundary layer is shown in figure 18(*a*). Consistent with the earlier observations concerning the upstream coherence based on wall pressure (see figure 16*a*), there is a weak crossing of the significance limit at low frequency in figure 18(*a*). The crossing is located in a region extending from wall-normal coordinate $z/\delta = 0.05$ to 0.4. There is thus possibly some weak relation between fluctuations in the upstream boundary layer at around this wall-normal location and the low-frequency shock motion. Summarizing the findings from figures 18 and 19, the

https://doi.org/10.1017/jfm.2011.560 Published online by Cambridge University Press

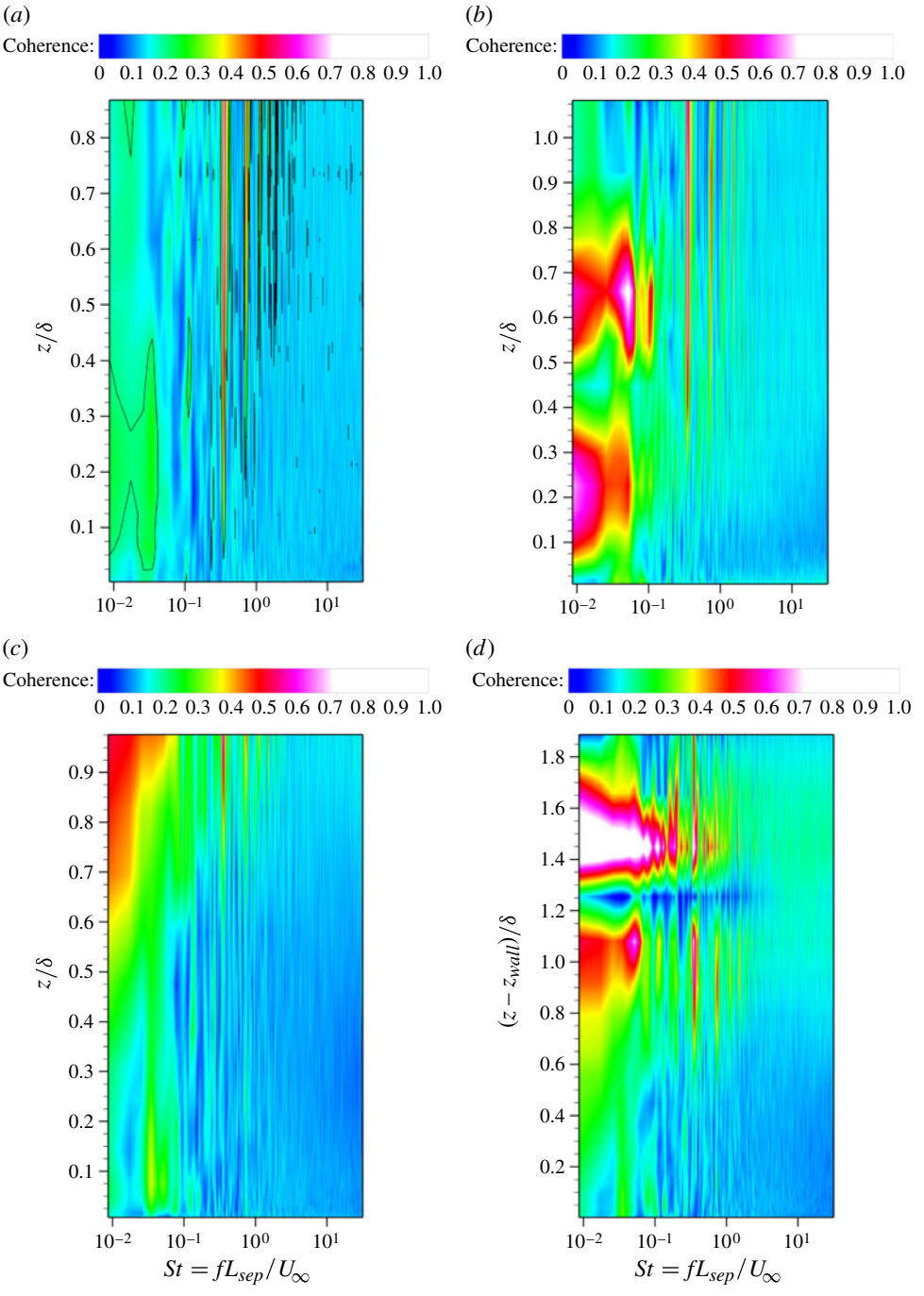


FIGURE 18. Coherence between the shock indicator signal and the mass flux signal at different grid planes: (*a*) grid plane 1; (*b*) grid plane 2; (*c*) grid plane 3; and (*d*) grid plane 4. See figure 5 for the location of the grid planes. Note that the plots have different ordinate scales. The black isoline shown in (*a*) is the 99.9 % significance limit of the coherence estimate.

https://doi.org/10.1017/jfm.2011.560 Published online by Cambridge University Press

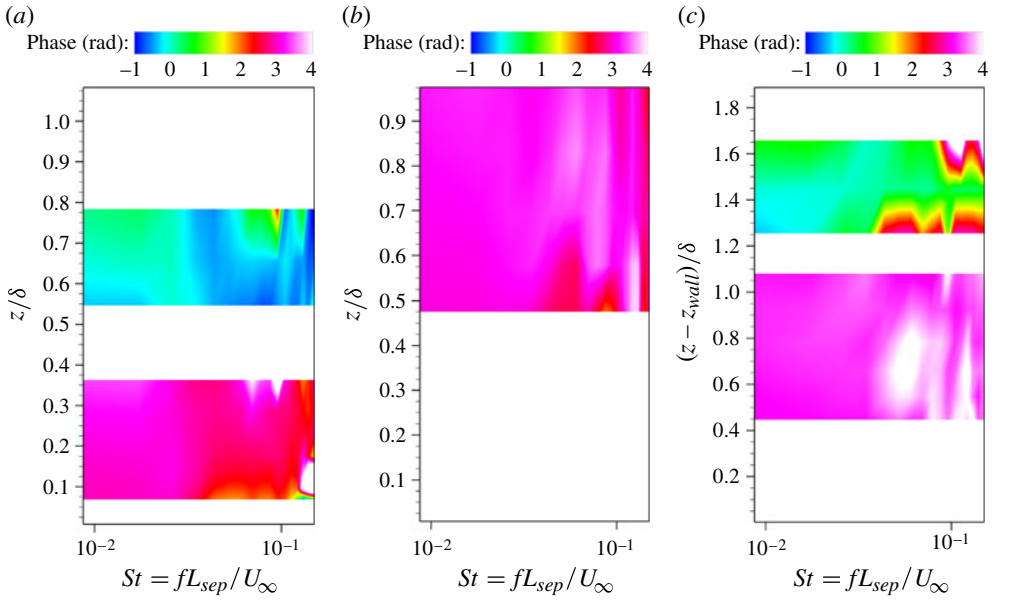


FIGURE 19. Phase between the shock indicator signal and the mass flux signal at different grid planes: (*a*) grid plane 2; (*b*) grid plane 3; and (*c*) grid plane 4. See figure 5 for the location of the grid planes. Note that the plots have different ordinate scales.

low-frequency shock motion in the free stream is statistically related to a large-scale mode in the downstream flow, which involves a flapping motion of the separated shear layer. In addition, there is possibly some weak influence of mass flux fluctuations in the incoming boundary layer on the low-frequency shock motion.

3.3. *Spanwise organization of the flow*

The flow visualizations in figures 7 and 8 have shown that, on an instantaneous basis, spanwise variation of the flow in the recirculation bubble and the shear layer exists. In this section, we investigate the spanwise organization of the flow statistically by means of the spanwise coherence and phase. The spanwise coherence is defined as the usual coherence between two time signals $s_1(t)$ and $s_2(t)$, where these signals are sampled at two different spatial locations in the flow field that are separated by a spanwise distance Δy, i.e. if the signal $s_1(t)$ is obtained at the spatial location (x, y, z), then $s_2(t)$ will be obtained at $(x, y + \Delta y, z)$. The spanwise phase is defined in an analogous manner as the phase between the two signals s_1 and s_2. In order to investigate the spanwise variation of the shock in the free stream, figure 20 plots the spanwise coherence and phase of the shock indicator signal for five different values of the separation distance Δy. The largest separation distance shown, $\Delta y/\delta = 0.97$, is (approximately) equal to half the spanwise extent of the computational domain. For small Δy, strong coherence is present across a wide range of frequencies, extending from the low frequencies associated with the shock unsteadiness to the high frequencies associated with turbulent fluctuations. As Δy is increased, the coherence at high (turbulent) frequencies decreases, whereas at low frequencies the coherence remains close to 1. At the maximum spanwise separation shown ($\Delta y/\delta = 0.97$), no significant coherence is present at high (turbulent) frequencies, indicating that these scales decorrelate across the spanwise width of the domain. At the low frequencies

https://doi.org/10.1017/jfm.2011.560 Published online by Cambridge University Press

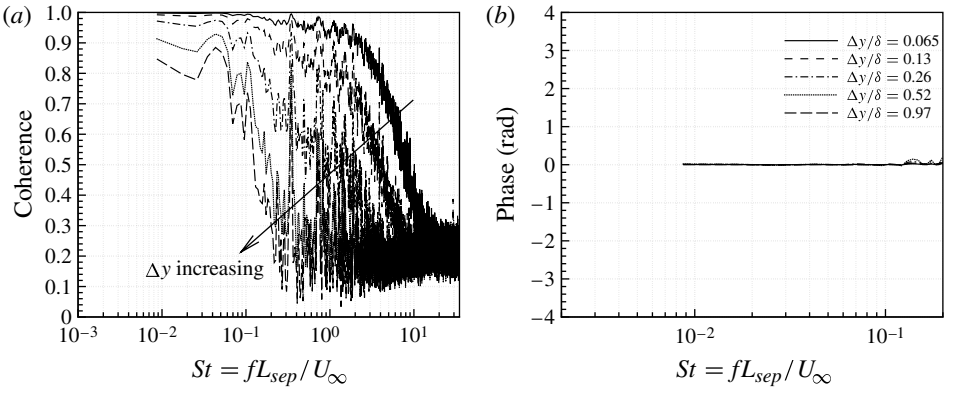


FIGURE 20. Spanwise coherence and phase of the shock indicator signal (i.e. the pressure signal obtained at $z/\delta = 1.4$ on grid plane 3). The key applies to both panels.

associated with the shock unsteadiness, however, the coherence remains close to 1, indicating an almost linear relationship between the signals across the spanwise extent of the domain. In addition, the signals are in phase at low frequency across the span. These observations indicate that the low-frequency motion of the shock in the free stream is essentially two-dimensional in the present simulation.

Figures 21 and 22 plot the spanwise coherence and phase based on wall pressure fluctuations at different streamwise locations. In the undisturbed boundary layer (figure 21*a*), there is some low-frequency coherence for small Δy, but for large Δy there is no significant low-frequency coherence. The absence of coherence in this case indicates that no significant spanwise-coherent low-frequency fluctuations are present in the incoming boundary layer. Figure 21(*b*) is obtained from the wall pressure near the foot of the separation shock; figure 21(*c*) is obtained in the recirculation bubble upstream of the corner; and figure 21(*d*) is obtained in the recirculation bubble at the corner. At these three locations, the behaviour is similar to that discussed for the shock indicator signal in figure 20. With increasing Δy, the high-frequency (turbulent) fluctuations decorrelate, whereas the low-frequency fluctuations remain strongly correlated across the span. In addition, the low-frequency fluctuations are in phase across the span. As for the shock motion in the free stream, it may thus be concluded that the low-frequency motions in the separated flow region are roughly two-dimensional.

Near reattachment (figure 22*a*), the wall pressure fluctuations appear to be more three-dimensional at low frequency. Some coherence is still present at low frequency and large Δy, but the level of coherence is lower than that observed in figures 20 and 21(*b–d*), indicating that three-dimensional effects are important near reattachment. Downstream of reattachment in the recovering boundary layer (figure 22*b*,*c*), the low-frequency wall pressure fluctuations appear to be essentially three-dimensional. There is little (if any) statistically significant coherence at low frequency and large Δy, indicating that the low-frequency fluctuations decorrelate across the span.

We conclude that at low frequency the shock in the free stream and the recirculation bubble are roughly two-dimensional, at least up to the corner. Near reattachment, some spanwise coherence is present but three-dimensional effects appear to be important.

The low-frequency unsteadiness is confined to be two-dimensional in the present simulation by the limited spanwise width of the computational domain. This is

https://doi.org/10.1017/jfm.2011.560 Published online by Cambridge University Press

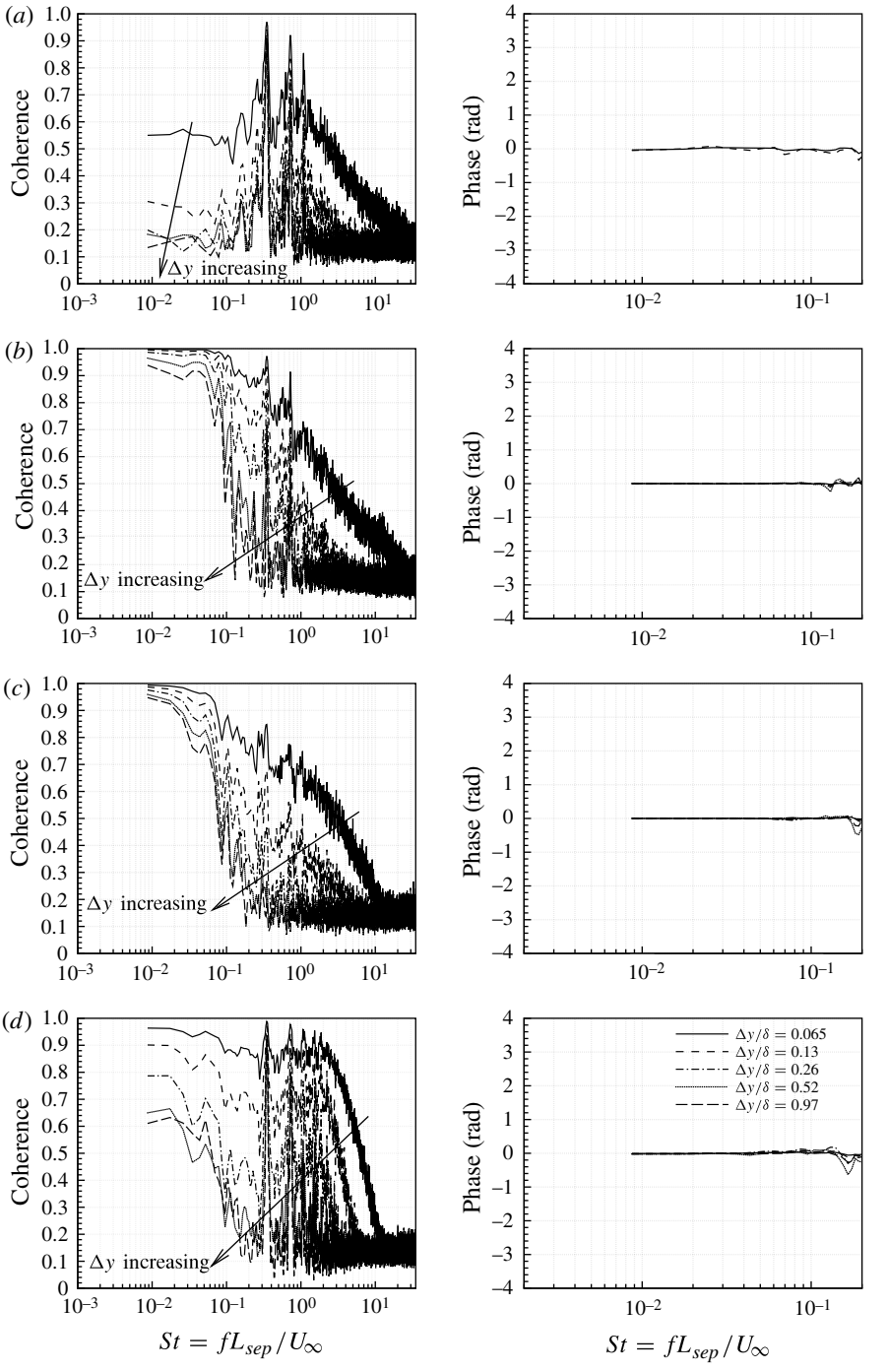


FIGURE 21. Spanwise coherence and phase of wall pressure at different streamwise locations: (*a*) $x/\delta = -3.97$; (*b*) $x/\delta = -2.48$; (*c*) $x/\delta = -1.53$; and (*d*) $x/\delta = 0$. The key applies to all panels.

https://doi.org/10.1017/jfm.2011.560 Published online by Cambridge University Press

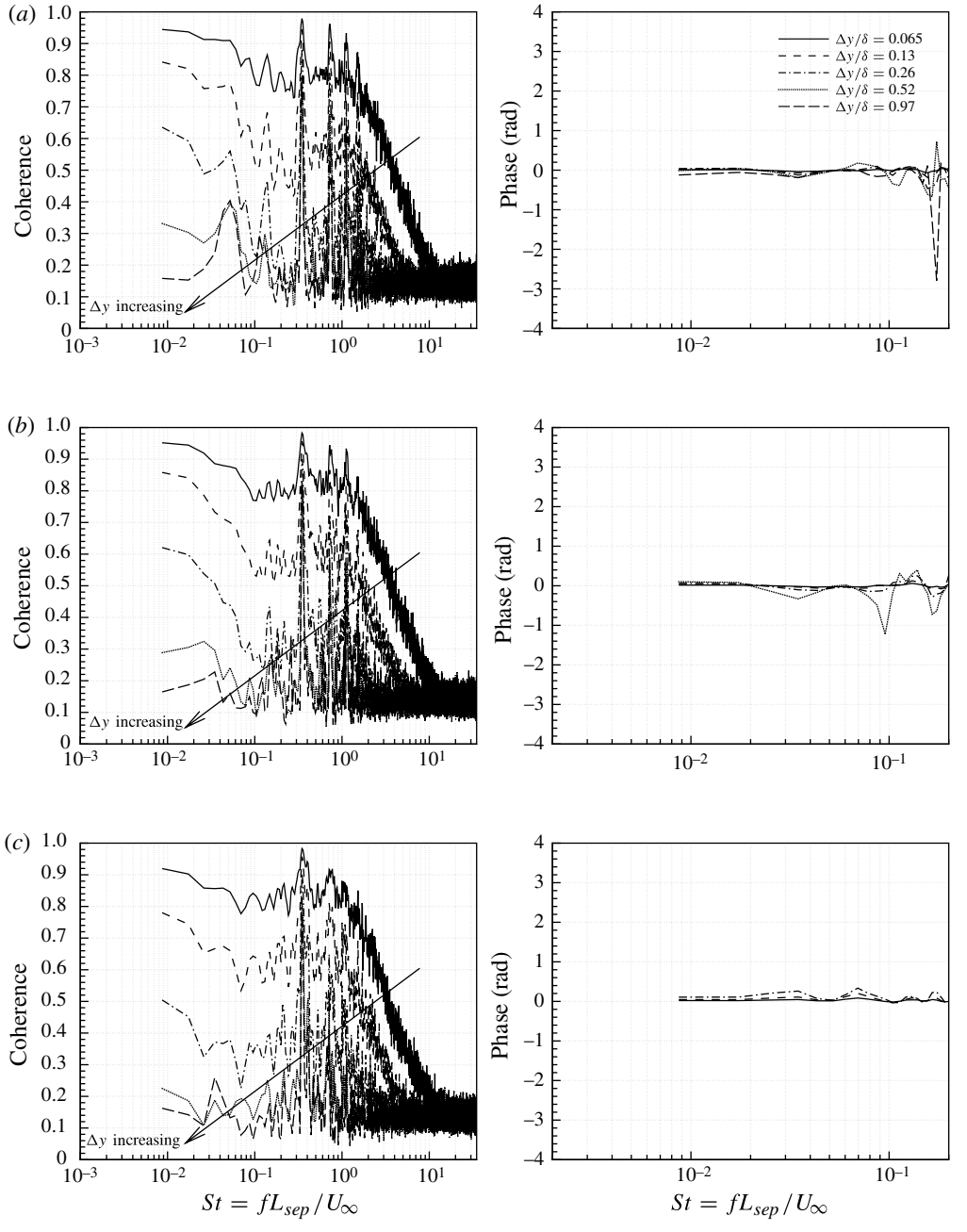


FIGURE 22. Spanwise coherence and phase of wall pressure at different streamwise locations: (*a*) $x/\delta = 1.05$; (*b*) $x/\delta = 2.43$; and (*c*) $x/\delta = 4.63$. The key applies to all panels.

a limitation of the present simulation in the sense that possible three-dimensional variations of the shock motion are not captured. The slow decay of the coherence levels at low frequency with increasing spanwise distance (see e.g. figure 21*b*) suggests that a much wider computational domain would be required to properly

https://doi.org/10.1017/jfm.2011.560 Published online by Cambridge University Press

resolve any such three-dimensional variations – see also the discussion in Wu & Martín (2008).

Since the low-frequency unsteadiness is roughly two-dimensional in the present simulation, it may be investigated from spanwise-averaged flow fields (as will be done in §§ 3.4 and 3.5). Since three-dimensional effects appear to be important near reattachment, observations and conclusions based on spanwise-averaged fields will only be made in the initial part of the interaction, up to the corner. Near reattachment, one needs to be careful about the interpretation of the spanwise-averaged fields. They are relevant in the sense that they show the global spanwise-mean flow in this region, which corresponds to the two-dimensional shock motion. However, through the process of spanwise averaging, the possibility exists either that relevant three-dimensional structure could be averaged out and missed altogether, or that it could be visible but only as projection onto the two-dimensional mean field.

3.4. *Low-pass filtered flow fields*

The statistical analysis presented in § 3.2 is based on linear statistical quantities (coherence and phase). In view of the possible nonlinearity of the unsteadiness, these linear statistical quantities could give a limited description of the low-frequency behaviour of the flow field. To further describe the unsteadiness, including nonlinear effects, low-pass filtered flow fields and their evolution in time are presented in this section.

Data from two additional DNS runs are used in this section, and these are referred to as detailed simulations 1 and 2. They are identical to the simulation described thus far in terms of numerical method, computational set-up and flow conditions, but the sampling frequency f_s at which the instantaneous three-dimensional flow field is output from the DNS is higher in the detailed simulations than in the original one: the sampling frequency is approximately $f_s\delta/U_\infty = 1$ in the original simulation, whereas it is approximately $f_s\delta/U_\infty = 10$ in the detailed simulations. This higher sampling frequency is necessary to obtain the time-resolved evolution of the spanwise-averaged flow field. Both detailed simulations are started from a flow field from the original simulation, and both are run for approximately $200\delta/U_\infty$ (i.e. one-fifth the duration of the original simulation).

The motion of the low-pass filtered separation point $\tilde{x}_s$ during simulation 1 is shown in figure 23. A finite impulse response (FIR) filter with cutoff Strouhal number 0.22 has been used for low-pass filtering. The order of the filter is 300 (samples), meaning that its duration in the time domain is approximately $30\delta/U_\infty$. At the start of the data record in figure 23, the low-pass filtered separation point is located at approximately $\tilde{x}_s/\delta = -2.3$ and moves upstream ($\mathrm{d}\tilde{x}_s/\mathrm{d}t < 0$). At $tU_\infty/L_{sep} = 45.5$, the separation point attains the most upstream location of the data record ($\tilde{x}_s/\delta = -2.55$), and subsequently it begins to move downstream ($\mathrm{d}\tilde{x}_s/\mathrm{d}t > 0$) at rapidly increasing speed. The maximum downstream-moving speed is attained near $tU_\infty/L_{sep} = 51$ and is significantly larger than the upstream-moving speed observed for $tU_\infty/L_{sep} < 45.5$. Following its rapid downstream motion, the separation point shows signs of stabilizing at a downstream location near $\tilde{x}_s/\delta = -1.95$ at approximately $tU_\infty/L_{sep} = 54$, only to move a short distance further downstream starting at $tU_\infty/L_{sep} = 58$. At $tU_\infty/L_{sep} = 60.5$, the separation point attains its most downstream location of $\tilde{x}_s/\delta = -1.85$, followed by a small upstream motion. The rest of the signal still shows some low-frequency oscillations but at smaller amplitude. The next pronounced upstream motion of the separation point occurs at

https://doi.org/10.1017/jfm.2011.560 Published online by Cambridge University Press

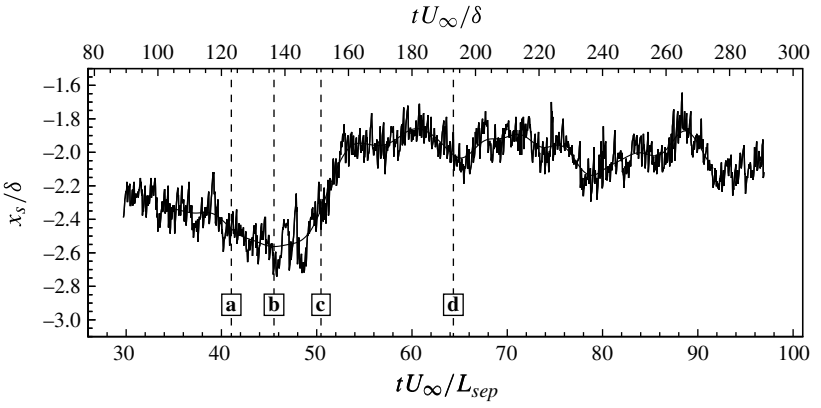


FIGURE 23. Location of spanwise-averaged separation point for detailed simulation 1. The low-pass filtered signal is also shown (cutoff Strouhal number 0.22). The vertical dashed lines with letters indicate the instants at which the flow fields in figure 24(*a–d*) are obtained.

approximately $tU_\infty/L_{sep} = 100$ and is not part of the detailed DNS but may be seen in the original DNS (see figure 9).

The separation point signal during the first half of simulation 1 may thus be described in summary as follows: a gradual upstream motion, followed by a rapid downstream motion and stabilization at a downstream location with subsequent mild upstream motion. The entire motion extends over a time of approximately $tU_\infty/L_{sep} = 35$. The evolution of the flow during this low-frequency motion may be seen from low-pass filtered flow fields. The starting point to obtain these fields is the time sequence of instantaneous three-dimensional flow fields sampled from the DNS. These are averaged in the spanwise direction, and the resulting fields in the (x, z) plane are filtered in time. The filtering is performed at each grid point in the (x, z) plane individually using the FIR filter described above.

Four low-pass filtered flow fields are shown in figure 24, and these fields correspond to the instants (*a–d*) indicated on the separation point signal in figure 23. In addition to the four key frames shown here, a supplementary movie of the entire time-resolved evolution of the low-pass filtered flow field during simulation 1 is available online at journals.cambridge.org/flm. The low-pass filtered flow fields are plotted as follows: an isocontour of pressure gradient $|\nabla p|\delta/p_\infty = 2$ indicates the shock, (u, w) streamlines indicate the state of the recirculating flow in the corner, and a colour contour map of the spanwise vorticity indicates the structure of the separated shear layer. In addition, the u velocity profile at $x/\delta = -4$ (shown as an inset) indicates the state of the inflow boundary layer.

In the first frame (figure 24*a*), the bubble is large and the shock is in an upstream location. The streamlines are fairly closely and uniformly spaced in the initial part of the separated shear layer ($-2 \leqslant x/\delta \leqslant -1$) and above the bubble, with a band of strong vorticity/shear extending from the separation point in the downstream direction, making an angle with the wall and lying above the recirculation bubble. The supplementary movie reveals that, at the instant corresponding to the first frame, the bubble is growing and the shock is moving upstream, consistent with the observations made on figure 23. There is some indication that the structure of the separated shear layer is beginning to change around the time of the second frame (figure 24*b*). The movie shows that the shock attains its most upstream location at that time (consistent

https://doi.org/10.1017/jfm.2011.560 Published online by Cambridge University Press

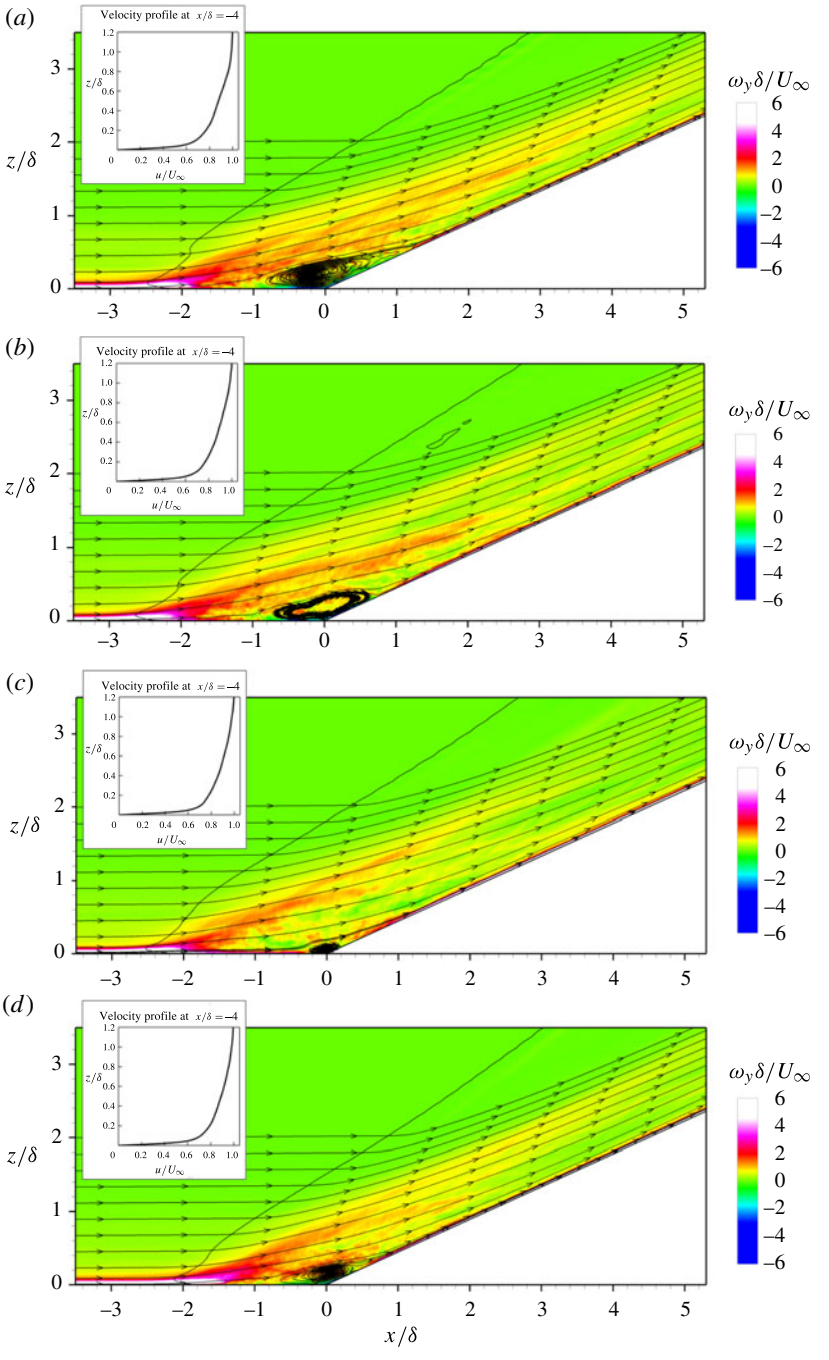


FIGURE 24. Spanwise-averaged low-pass filtered flow fields at the instants indicated in figure 23.

with the observations made on figure 23) and that, in the initial part of the shear layer ($-2 \leqslant x/\delta \leqslant -1$), the streamline shown closest to the wall is pushed towards the wall as it diverges from its neighbour further away in the flow. Concurrently, a

https://doi.org/10.1017/jfm.2011.560 Published online by Cambridge University Press

second region of high vorticity develops along the wall downstream of separation in addition to the main branch of strong vorticity in the flow, and the recirculation bubble begins to shrink. The divergence of the streamlines in the initial separated shear layer and the development of a second region of high vorticity along the wall are visible, in their initial stages, in figure 24(*b*). The third frame (figure 24*c*) is obtained around the time when the separation point is moving downstream at maximum speed (see the separation point signal in figure 23). The movie shows that the recirculation bubble is rapidly shrinking at this time and the shock is moving downstream. The changes in the structure of the shear layer that are visible in their initial stages in figure 24(*b*) are pronounced in figure 24(*c*): the region of strong vorticity downstream of separation is bifurcated with one branch in the flow, making an angle with the wall, and another branch along the wall. In the fourth frame (figure 24*d*), the shock is stabilized in a relatively downstream location, the bubble has recovered to some intermediate size, and the bifurcation of the shear layer has disappeared. It may be noted that the general structure of the flow in figure 24(*a*,*d*) is similar (although there are differences in bubble size and shock position, i.e. the flow field length scale is different).

A direct comparison of figure 24(*a*) (bubble growth phase) with figure 24(*c*) (bubble collapse phase) shows the different structure in the flow downstream of separation depending on the phase of the shock motion. Whereas the shock is in a fairly similar position in both figures, the structure of the flow downstream of separation is different: single branch of strong vorticity in the flow versus bifurcated structure with two branches of strong vorticity, the second branch being along the wall; large versus small bubble; closely and uniformly spaced streamlines downstream of separation versus diverging streamlines. To further qualify the low-frequency evolution of the shear layer, profiles of u velocity and spanwise vorticity ω_y are plotted in figures 25–28, where the four figures correspond to the instants discussed thus far. The shear layer profiles in figure 25 generally resemble those of a plane mixing layer with a low-speed side near the wall and a high-speed side in the free stream, connected by a profile that has one global inflection point located away from the wall approximately in the middle of the layer. In figure 26, there is some indication of departures from this type of profile. At $x/\delta = -1.5$, the ω_y profile (figure 26*c*) shows three extrema: a maximum near the wall, followed further above the wall by a minimum and yet further above the wall by another maximum. The u velocity profile at the same location (figure 26*a*) shows a departure from the type of profile seen in figure 25(*a*) in the sense that it contains a high-velocity 'bulge' near the wall. Similar but more pronounced high-velocity 'bulges' are visible in all profiles from $x/\delta = -1.5$ to -0.5 in figure 27(*a*), and these profiles look distinctly different from those in figure 25(*a*). In fact, the flow in figure 27 reattaches in a region downstream of separation and upstream of the corner. In the range $x/\delta = -1.5$ to -0.5, the vorticity profiles show large values close to the wall, followed some distance above the wall by a minimum and yet further above the wall by another maximum. The profiles in figure 28 have returned to the type of profile seen in figure 25 showing mixing-layer-like behaviour with a single global inflection point in the layer.

The low-pass filtered C_f distributions for instants (*a–d*) are shown in figure 29. During the bubble growth phase (figure 29*a*), a single region of separated flow is present, which extends over the streamwise interval $x/\delta \in [-2.46, 1.26]$. A different structure is observed in figure 29(*c*) when the bubble collapses: a large-scale region of attached flow is present, which extends over the streamwise interval $x/\delta \in (-1.95, -0.47)$. This region of attached flow splits the bubble into two disjoint patches of separated flow: one is located near the separation shock foot

https://doi.org/10.1017/jfm.2011.560 Published online by Cambridge University Press

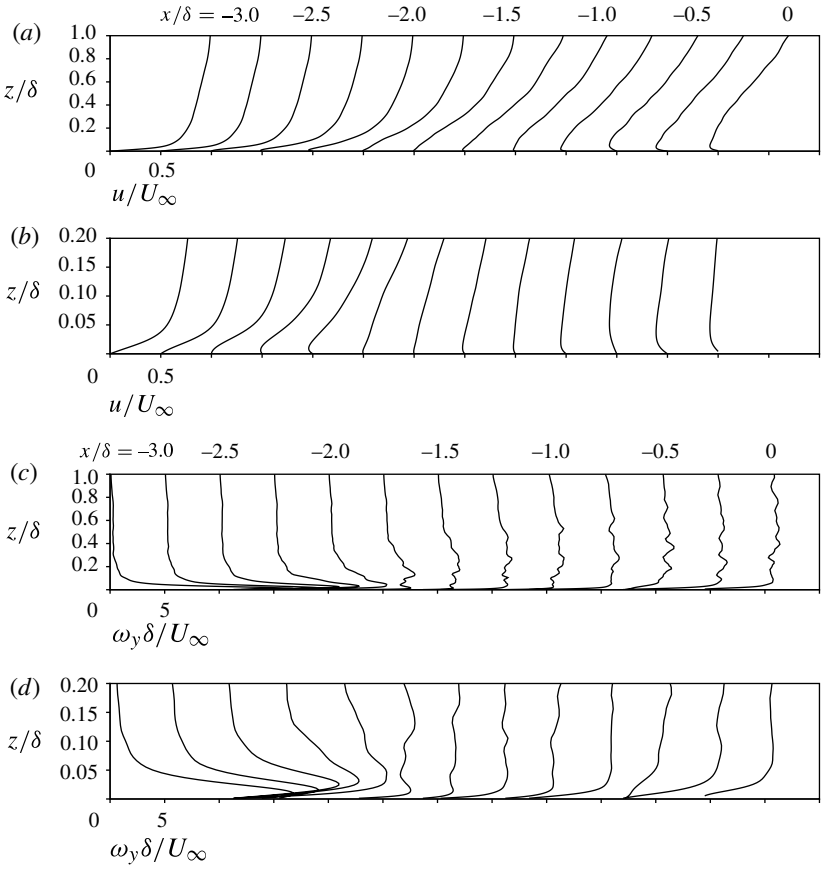


FIGURE 25. Profiles corresponding to the low-pass filtered flow field shown in figure 24(*a*): (*a*) streamwise velocity; (*b*) detail of streamwise velocity near wall; (*c*) spanwise vorticity; and (*d*) detail of spanwise vorticity near wall.

and extends over the streamwise interval $x/\delta \in [-2.33, -1.95]$; and the other is located in the region surrounding the corner and extends over the streamwise interval $x/\delta \in [-0.47, 0.70]$. The presence of this region of attached flow is consistent with the behaviour of the vorticity field discussed above: the appearance of a second branch of large positive vorticity near the wall as the bubble collapses is consistent with the flow reattaching in this region.

The observations made above about the low-frequency motion in detailed simulation 1 are confirmed by detailed simulation 2. The motion of the separation point in detailed simulation 2 is shown in figure 30. The signal displays a series of upstream–downstream motions at a Strouhal number of approximately 0.1. While this frequency may be somewhat higher than the central frequency of the shock motion, it falls within the broadband peak surrounding the central frequency (see figure 12) and it is disjoint from any other time scale in the flow (rescaling or turbulence); the motion in figure 30 is thus attributable to the low-frequency unsteadiness.

Four low-pass filtered flow fields for detailed simulation 2 are shown in figure 31. In addition, a supplementary movie of the entire time-resolved evolution of the low-pass filtered flow field during simulation 2 is also available online. Instants (*a*) and (*c*) are

https://doi.org/10.1017/jfm.2011.560 Published online by Cambridge University Press

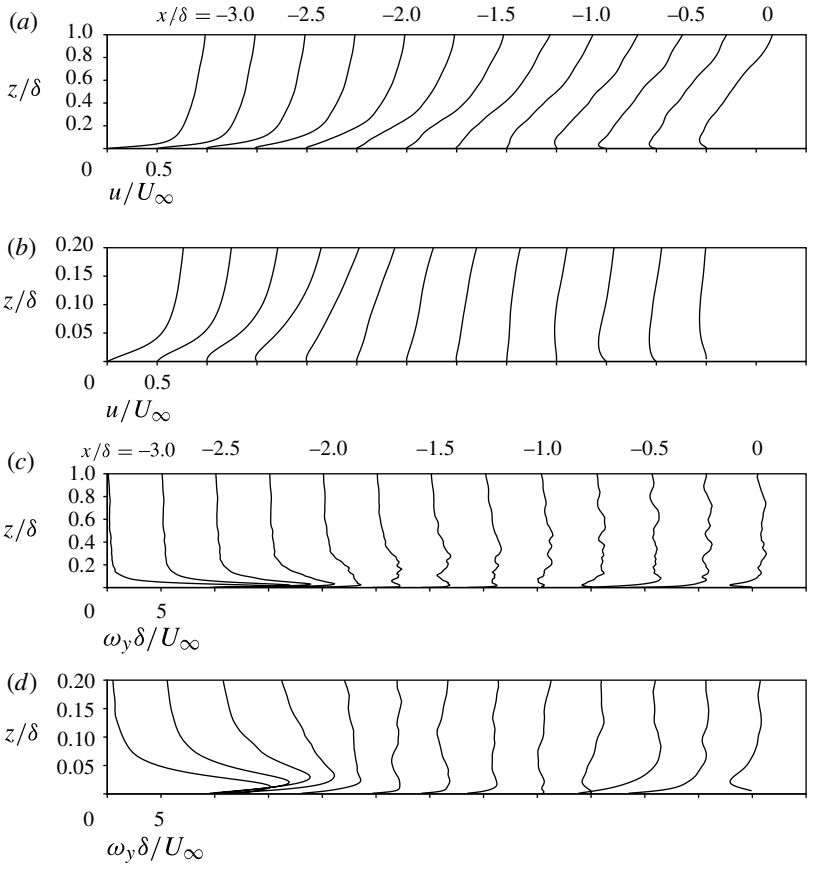


FIGURE 26. Same as figure 25, except that the profiles correspond to the low-pass filtered flow field shown in figure 24(*b*).

obtained as the separation point moves downstream ($\mathrm{d}\tilde{x}_s/\mathrm{d}t > 0$; see figure 30). At these instants, the low-pass filtered fields (figure 31*a*,*c*) show a bifurcated shear layer structure similar to that previously observed in figure 24(*c*). In addition, the movie shows that, at the time of figure 31(*a*,*c*), the recirculation bubble is shrinking and the shock is moving downstream. Instants (*b*) and (*d*) are obtained as the separation point moves upstream ($\mathrm{d}\tilde{x}_s/\mathrm{d}t < 0$; see figure 30). The corresponding low-pass filtered flow fields (figure 31*b*,*d*) are similar to those previously discussed in figure 24(*a*,*d*). The recirculation bubble is fairly large, and the streamlines are fairly closely and uniformly spaced in the initial separated shear layer and above the bubble. A single branch of strong vorticity extends from separation downstream into the flow, making an angle with the wall and lying above the recirculation bubble. The movie shows that the bubble is growing and the shock is moving upstream at these instants.

The velocity and vorticity profiles for the four instants discussed are shown in figures 32–35. Figures 33 and 35 show shear layer velocity profiles that resemble those of a plane mixing layer, whereas the profiles in figures 32 and 34 show the previously discussed departures from this type of profile. In figure 32, the profiles have high-velocity 'bulges' near the wall for $x/\delta = -1.25$ to -0.5, and in figure 34 these are visible for $x/\delta = -1.5$ to -0.75. The C_f distributions for the four instants discussed

https://doi.org/10.1017/jfm.2011.560 Published online by Cambridge University Press

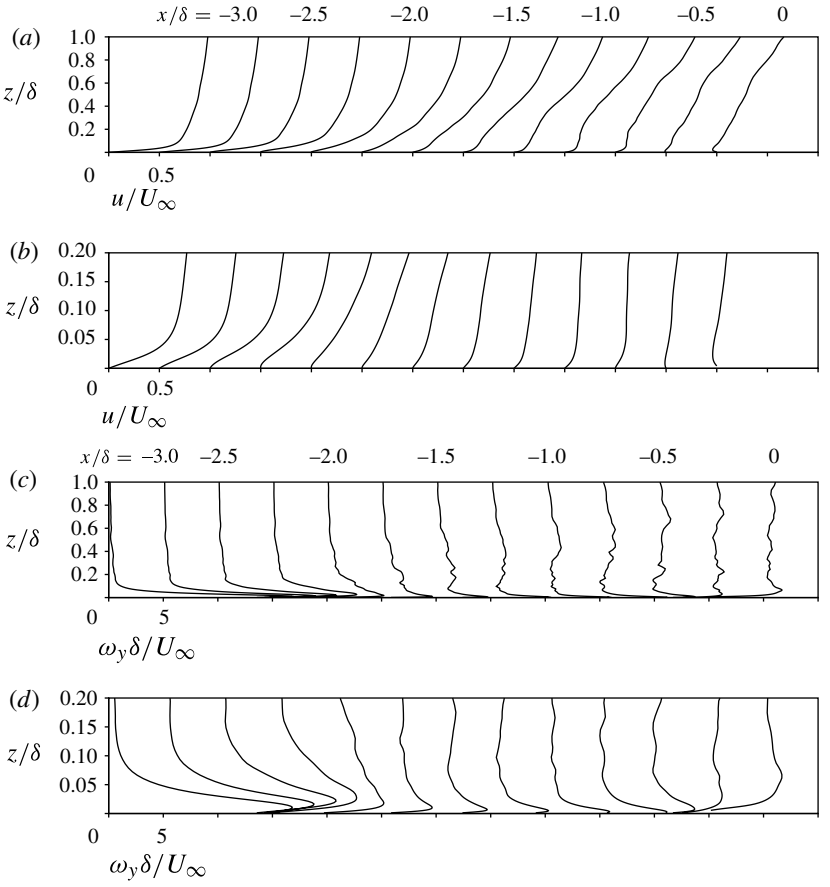


FIGURE 27. Same as figure 25, except that the profiles correspond to the low-pass filtered flow field shown in figure 24(*c*).

are shown in figure 36. During the bubble growth phase (figure 36*b*,*d*), a single region of separated flow is present, whereas during the bubble collapse phase (figure 36*a*,*c*), a large-scale region of attached flow is present inside the bubble. This region of attached flow extends approximately over the streamwise interval $x/\delta \in (-1.5, -0.5)$.

Two main observations have been made above about the low-frequency motion, and these may be summarized as follows (see also the schematic in figure 37). (i) The motion of the shock and the pulsation of the bubble are related. The growth of the bubble is associated with the shock moving upstream, whereas the shrinking of the bubble is associated with the shock moving downstream. (ii) The structure of the separated shear layer changes depending on the phase of the low-frequency motion. As the bubble grows, a single branch of strong vorticity exists downstream of separation, making an angle with the wall and lying above the recirculation bubble. The shear layer velocity profiles resemble those of a plane mixing layer with a single inflection point. As the bubble shrinks, the vorticity field downstream of separation has a bifurcation with a second branch of strong vorticity along the wall where the flow is reattaching. The bubble breaks. The shear layer velocity profiles contain a high-velocity 'bulge' near the wall and are qualitatively different from plane mixing layer profiles. The results presented in this section thus show that the low-frequency

https://doi.org/10.1017/jfm.2011.560 Published online by Cambridge University Press

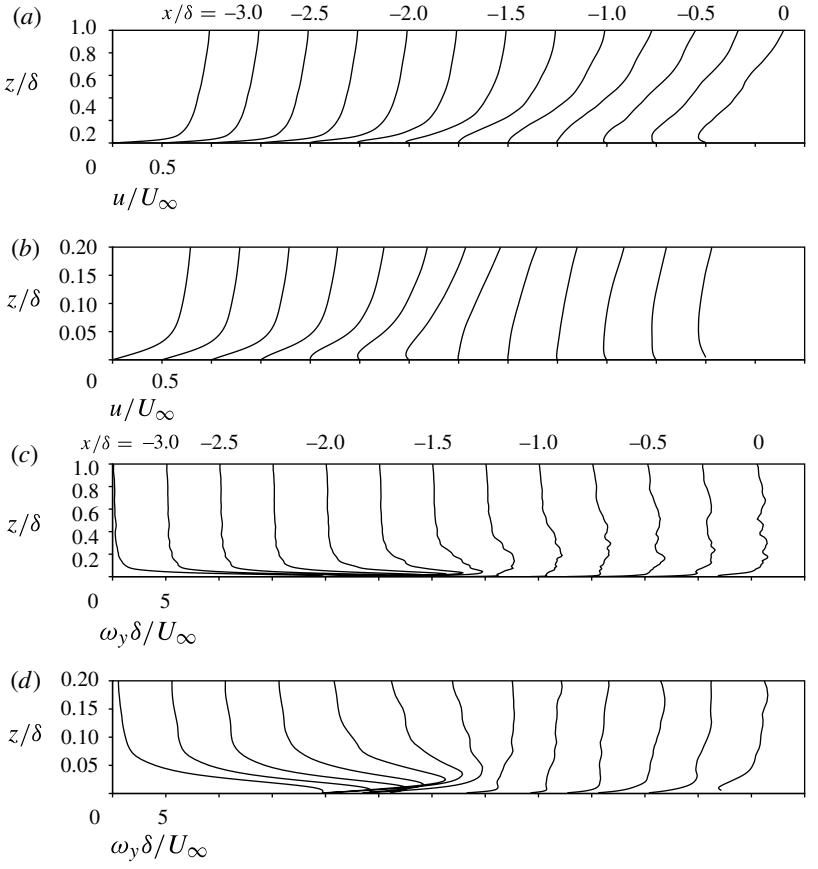


FIGURE 28. Same as figure 25, except that the profiles correspond to the low-pass filtered flow field shown in figure 24(*d*).

pulsations of the downstream separated flow involve changes in the flow structure and are not simply changes in the flow field length scale.

3.5. *Low-frequency modulation of energetic turbulent structures in the shear layer*

The shear layer profiles change depending on the phase of the low-frequency unsteadiness, and this may be expected to produce some changes in the properties of the energetic turbulent structures in the shear layer. In order to investigate whether such low-frequency modulation occurs, data from an additional detailed DNS are used in this section, and this is referred to as detailed simulation 3. This simulation is identical to the simulations described thus far except that the sampling frequency f_s at which the instantaneous three-dimensional flow field is output from the DNS is higher; the sampling frequency for detailed simulation 3 is approximately $f_s\delta/U_\infty = 50$, which is necessary to obtain the time-resolved evolution of the flow field at individual grid points.

The motion of the low-pass filtered separation point $\tilde{x}_s$ during simulation 3 is shown in figure 38, and the four low-pass filtered flow fields corresponding to the instants (*a–d*) are shown in figure 39. These instants occur during a segment of the signal where the separation point undergoes an almost sinusoidal upstream–downstream

https://doi.org/10.1017/jfm.2011.560 Published online by Cambridge University Press

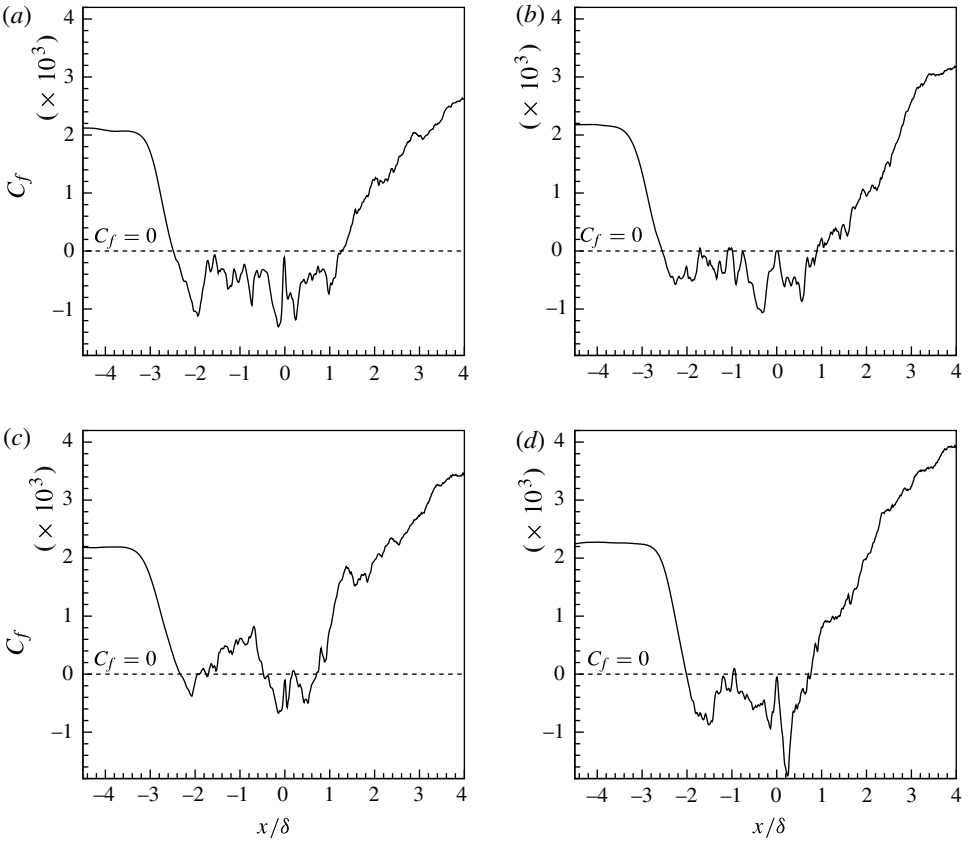


FIGURE 29. Low-pass filtered C_f distribution at the instants indicated in figure 23.

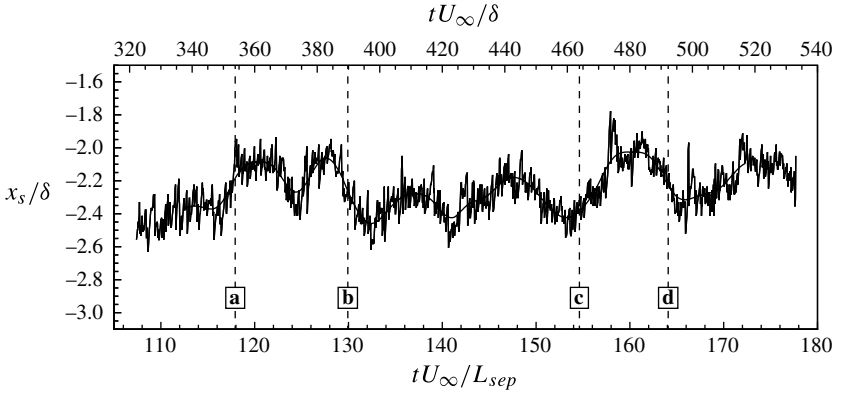


FIGURE 30. Location of spanwise-averaged separation point for detailed simulation 2. The low-pass filtered signal is also shown (cutoff Strouhal number 0.22). The vertical dashed lines with letters indicate the instants at which the flow fields in figure 31(*a–d*) are obtained.

https://doi.org/10.1017/jfm.2011.560 Published online by Cambridge University Press

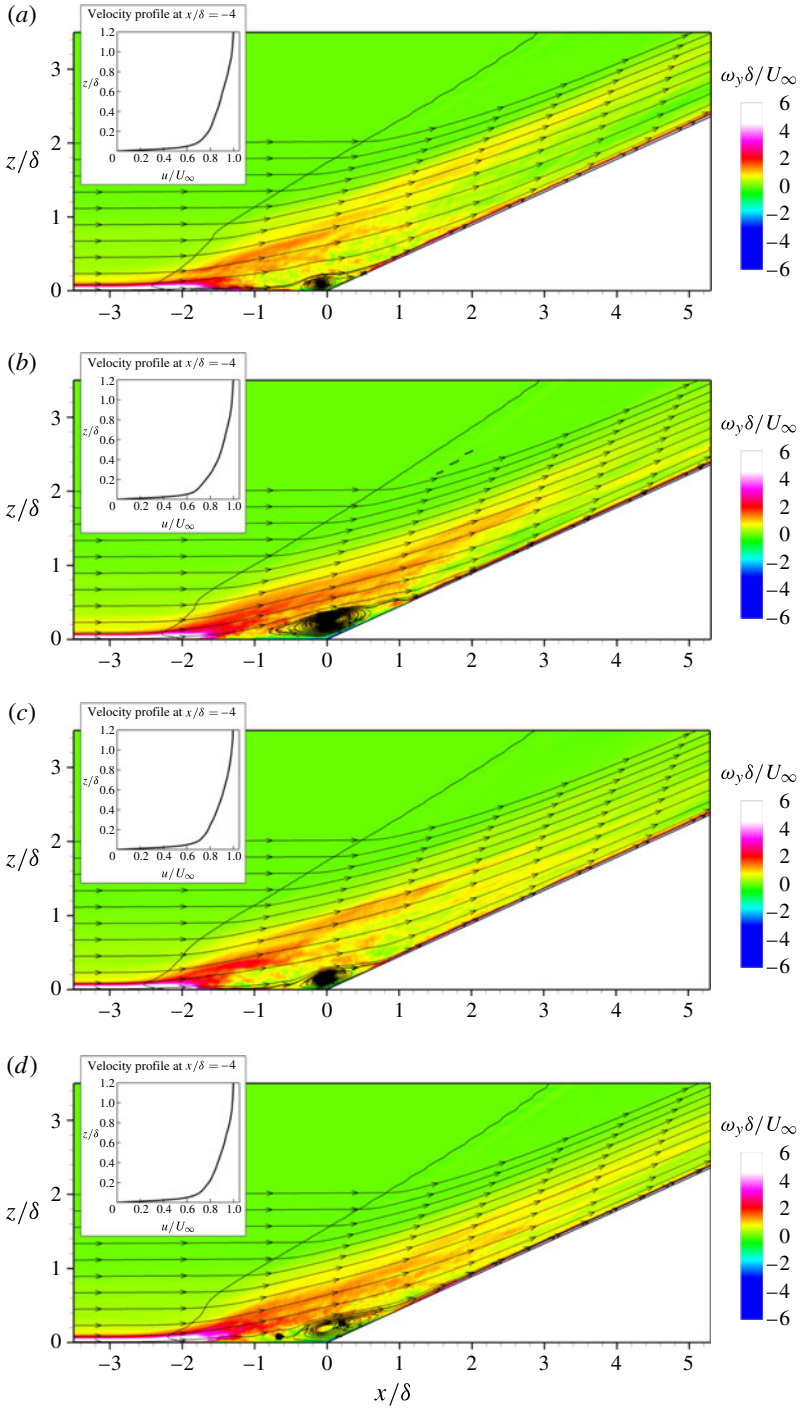


FIGURE 31. Spanwise-averaged low-pass filtered flow fields at the instants indicated in figure 30.

https://doi.org/10.1017/jfm.2011.560 Published online by Cambridge University Press

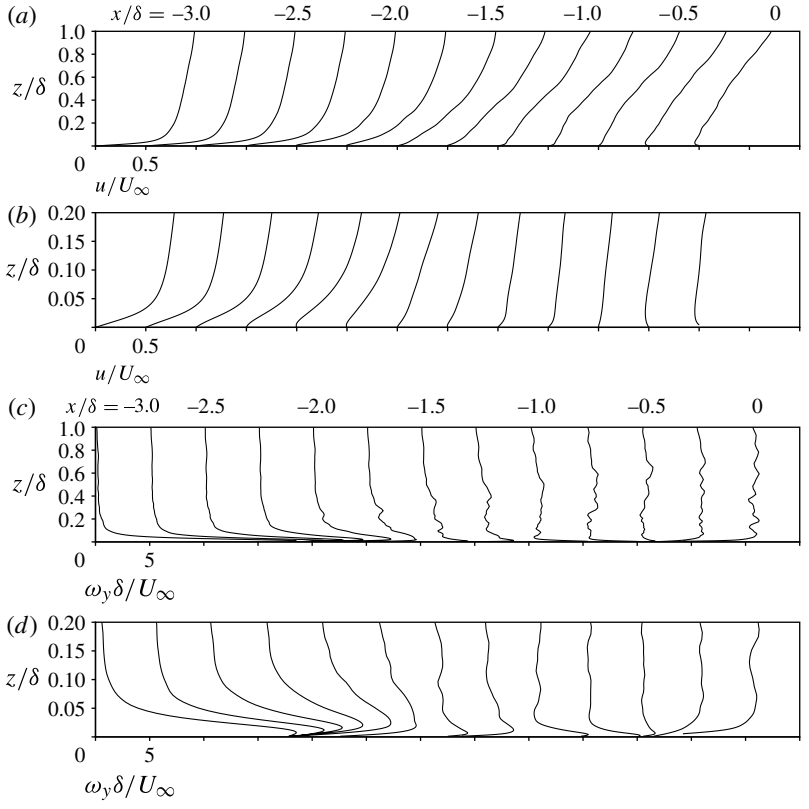


FIGURE 32. Profiles corresponding to the low-pass filtered flow field shown in figure 31(*a*): (*a*) streamwise velocity; (*b*) detail of streamwise velocity near wall; (*c*) spanwise vorticity; and (*d*) detail of spanwise vorticity near wall.

motion at a frequency of approximately $St = 0.1$. The low-pass filtered flow fields (figure 39) are plotted as follows: like in the plots in § 3.4 above, an isocontour of pressure gradient $|\nabla p|\delta/p_\infty = 2$ indicates the shock, and (u, w) streamlines indicate the state of the recirculating flow in the corner; in contrast to the plots in § 3.4, the colour contour map is of in-plane turbulent kinetic energy (TKE) $(u'^2 + w'^2)/2U_\infty^2$ and indicates the intensity of the turbulent fluctuations in the flow field. In order to retain only those fluctuations associated with the turbulent structures and discard fluctuations associated with the low-frequency unsteadiness, the in-plane TKE is calculated as follows. At each grid point, the time sequence of flow fields sampled from the DNS is high-pass filtered in time. The high-pass filter is an FIR filter with cutoff Strouhal number 0.3, which discards all energy associated with the low-frequency unsteadiness. The resulting high-pass filtered velocity fluctuations u' and w' are used to calculate the in-plane TKE at each grid point. The resulting field is spanwise-averaged and low-pass filtered by means of the low-pass FIR filter described in § 3.4.

The low-pass filtered fields in figure 39 show that the largest values of TKE occur approximately in the middle of the separated shear layer: there is a band of largest TKE that has its origin at the shock foot and extends in the downstream direction, lying above the recirculation bubble. Relatively large values of TKE are also observed past reattachment in the downstream recovering flow. These observations of large

https://doi.org/10.1017/jfm.2011.560 Published online by Cambridge University Press

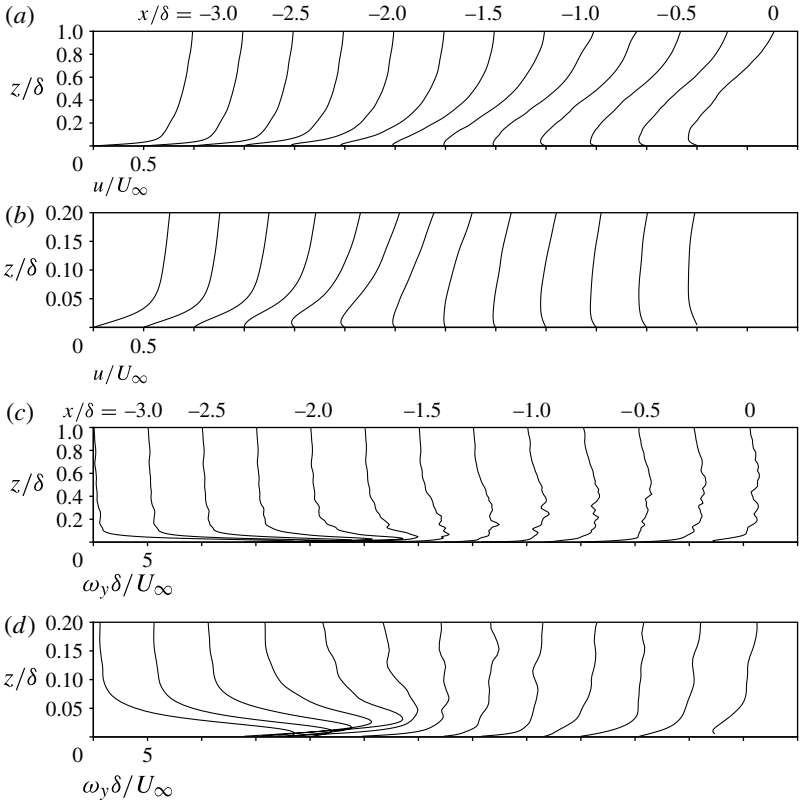


FIGURE 33. Same as figure 32, except that the profiles correspond to the low-pass filtered flow field shown in figure 31(*b*).

turbulence intensity in the middle of the separated shear layer and in the downstream flow are similar to those made from mean flow fields in the reflected shock case (e.g. Dupont *et al.* 2008; Souverein *et al.* 2010). The large turbulence intensity in this region can be attributed to the formation of energetic turbulent structures in the separated shear layer and subsequent shedding of these structures into the downstream flow.

The turbulence intensity in the shear layer varies at low frequency during simulation 3, with weak intensities corresponding to small recirculation bubbles, and vice versa. Looking at the initial separated shear layer ($-2 \leqslant x/\delta \leqslant -1$), the values of TKE are smaller in figure 39(*a*,*c*) than in figure 39(*b*,*d*). Instants (*a*) and (*c*) are obtained when the low-pass filtered separation point $\tilde{x}_s$ attains a maximum, i.e. when the separation point is at its most downstream location and the recirculation bubble is small. Instants (*b*) and (*d*) are obtained when $\tilde{x}_s$ attains a minimum, i.e. when the separation point is at its most upstream location and the recirculation bubble is large. The intensity of the energetic turbulent structures in the shear layer is thus dependent on the phase of the low-frequency unsteadiness, with weak intensities corresponding to small bubbles, and vice versa. This behaviour is consistent with conditionally averaged PIV fields obtained by Hou, Clemens & Dolling (2003) in a Mach 2 compression ramp. They find that the level of streamwise velocity fluctuations u' is significantly

https://doi.org/10.1017/jfm.2011.560 Published online by Cambridge University Press

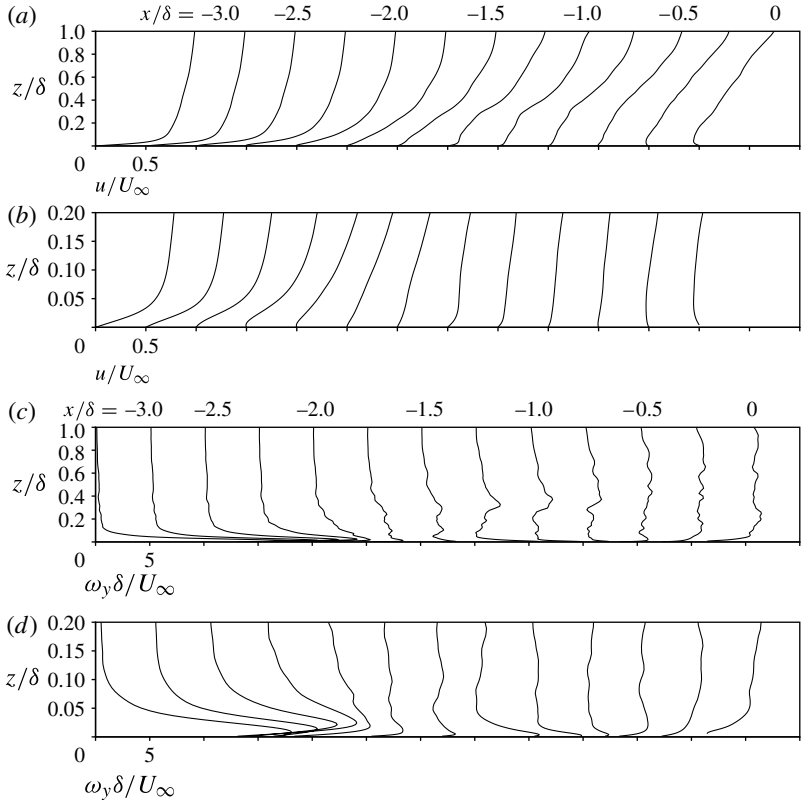


FIGURE 34. Same as figure 32, except that the profiles correspond to the low-pass filtered flow field shown in figure 31(*c*).

higher when the shock is located in an upstream position than when it is located in a downstream position (see Hou *et al.* 2003, figure 11).

4. Physical origin of low-frequency unsteadiness

The statistical analysis (§ 3.2) and the analysis of the low-pass filtered flow field (§ 3.4) show that a large-scale low-frequency mode is present in the flow. The mode involves the separated shear layer, the recirculation bubble and the shock wave; a weak relation with the incoming boundary layer is also observed.

This weak relation with the incoming boundary layer is consistent with the observations by Piponniau *et al.* (2009) in experiments of Mach 2.3 reflected shock interactions that the incoming boundary layer velocity profile, conditioned on the size of the recirculation bubble, is slightly fuller for small bubbles and less full for large bubbles. In the experiments, as in the present DNS, the effect is weak, and it may be concluded that 'small variations in the upstream conditions seem unlikely to be the main reason for the large-amplitude motions of the separated bubble' (Piponniau *et al.* 2009). The weak statistical relation between the incoming boundary layer and the low-frequency unsteadiness could be due to a weak direct effect on the shock, or it could indicate a weak modulation of the dynamics of the bubble and shear layer by upstream perturbations, or both.

https://doi.org/10.1017/jfm.2011.560 Published online by Cambridge University Press

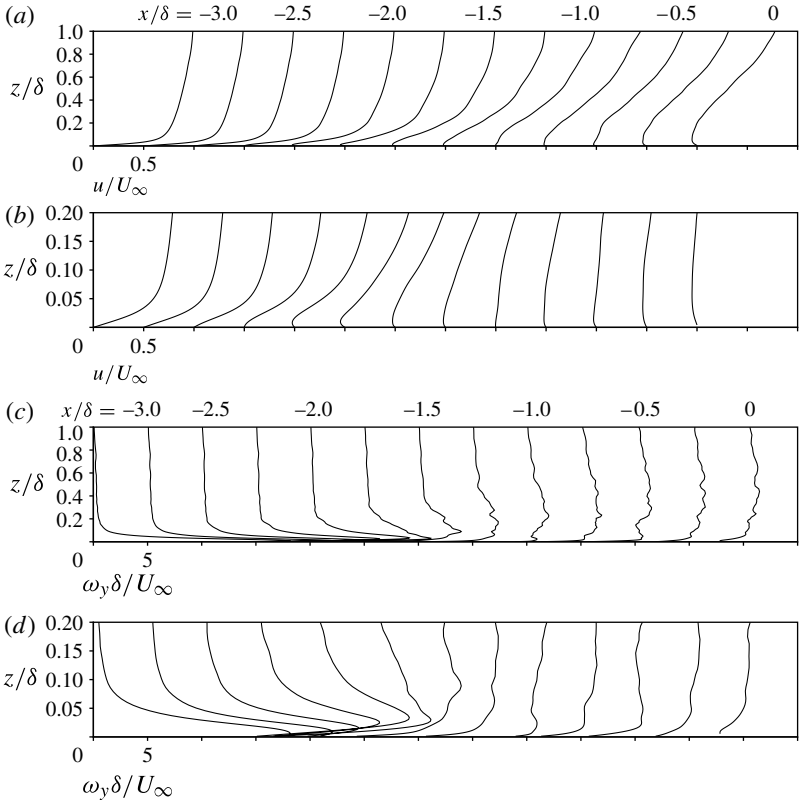


FIGURE 35. Same as figure 32, except that the profiles correspond to the low-pass filtered flow field shown in figure 31(*d*).

The observed low-frequency mode involves a breathing motion of the recirculation bubble and an associated flapping motion of the shear layer (see §§ 3.2 and 3.4). Significant 'distortions' of the velocity field in the initial part of the interaction, upstream of the corner, are observed at low frequency (§ 3.4). The nature of the flow in this region changes depending on whether the bubble is growing or collapsing (see the schematic in figure 37). The observed low-frequency mode may be regarded as the output response of the STBLI system (where this system is defined by the governing equations together with the appropriate boundary conditions and flow parameters). Since the turbulence may be viewed as a continuous forcing on the system, it is difficult to make the distinction between the intrinsic, unforced dynamics of the system (i.e. an instability) and the extrinsic, forced dynamics. Note also that the response may be called global since the system has more than one inhomogeneous spatial direction (it has two, the streamwise and the wall-normal direction). The observed response probably has to be linked to a global instability in the downstream separated flow, providing a driving mechanism for the low-frequency unsteadiness.

In this regard we note that the observed response has a similar C_f distribution through the interaction as the unstable global mode found by Touber & Sandham (2009). As mentioned before, they perform a linear stability analysis of the mean flow obtained from LES of a Mach 2.3 reflected shock interaction. They find an exponentially growing two-dimensional global mode. The effect of the global mode on

https://doi.org/10.1017/jfm.2011.560 Published online by Cambridge University Press

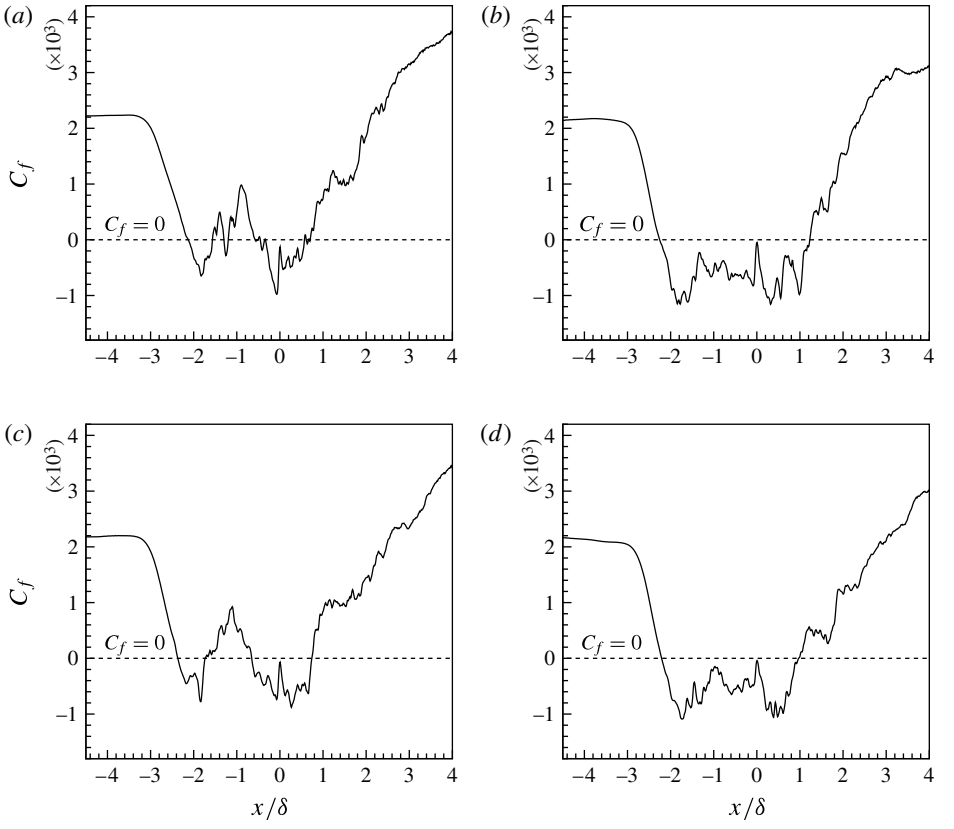


FIGURE 36. Low-pass filtered C_f distribution at the instants indicated in figure 30.

the separation bubble is either to break it up or to enhance separation in the initial part of the bubble, depending on the sign of the amplitude function. This behaviour is similar to that observed in the present work. In the case of a broken bubble, the C_f distribution of the global mode given in Touber & Sandham (2009) is strongly reminiscent of the C_f distribution observed in the present DNS. The similarity may be seen by comparing figures 29(*c*), 36(*a*,*c*) and 40 in the present paper with figure 15 in Touber & Sandham (2009). In view of this similarity, the low-frequency response observed here could be linked to a global instability in the downstream separated flow.

Several of the mechanisms that have been proposed to explain the low-frequency unsteadiness in terms of the dynamics of the separated flow are based on a control volume view of the recirculation bubble: the breathing of the bubble is explained by a time-varying net flux of mass into, or out of, the bubble. The physical processes that are identified as causing a flux of mass into, or out of, the bubble are the shear layer entrainment, which removes mass from the bubble, and the injection from the downstream flow, which supplies mass to the bubble. Piponniau *et al.* (2009) proposed the following physical scenario: shear layer entrainment causes a gradual reduction of mass in the bubble until a significant deficit of mass exists and a fresh amount of reverse flow is supplied from downstream, resulting in large-scale breathing of the bubble. A similar type of scenario was proposed by Eaton & Johnston (1982) in the context of incompressible separated flows. They suggested that the low-frequency

https://doi.org/10.1017/jfm.2011.560 Published online by Cambridge University Press

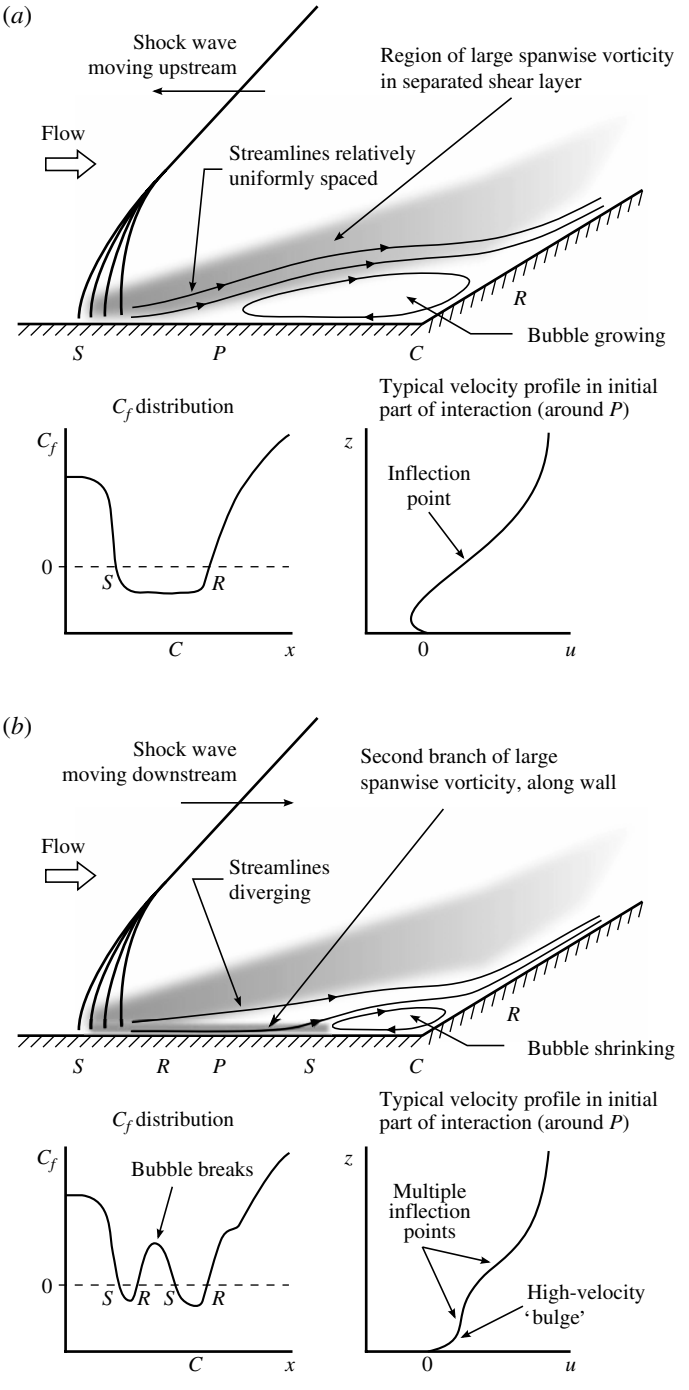


FIGURE 37. Schematics of the different flow structure observed depending on the phase of the low-frequency motion: (*a*) bubble growth phase; and (*b*) bubble collapse phase.

https://doi.org/10.1017/jfm.2011.560 Published online by Cambridge University Press

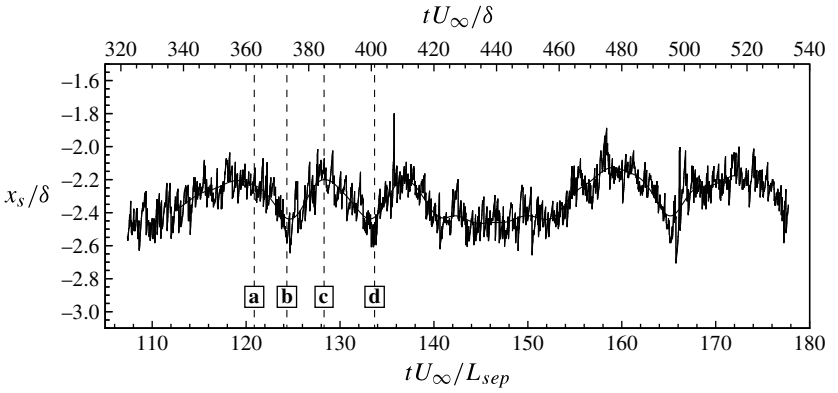


FIGURE 38. Location of spanwise-averaged separation point for detailed simulation 3. The low-pass filtered signal is also shown (cutoff Strouhal number 0.22). The vertical dashed lines with letters indicate the instants at which the flow fields in figure 39(*a–d*) are obtained.

unsteadiness is 'probably caused by an instantaneous imbalance between shear-layer entrainment from the recirculating zone on one hand and reinjection of fluid near reattachment on the other. For example, an unusual event may cause a short-term breakdown of the spanwise vortices in the shear layer. The entrainment rate would be temporarily decreased, while the reinjection rate remained constant. This would cause an increase in the volume of recirculating fluid, thus moving the shear layer away from the wall and increasing the short-time-averaged reattachment length.' As shown in § 3.5, there is evidence in the present DNS results that the properties of the shear layer structures vary at low frequency. We observe a link between the turbulence intensity in the shear layer and the size of the recirculation bubble: large values of turbulence intensity in the shear layer are observed for large bubbles and, conversely, small values of turbulence intensity are observed for small bubbles. This shows that the low-frequency unsteadiness involves a low-frequency modulation of the development of energetic turbulent structures in the shear layer and hence probably a modulation of shear layer entrainment.

5. Conclusions

We have analysed the low-frequency unsteadiness in the DNS of a 24° compression ramp interaction at Mach 2.9. The unsteadiness involves large-scale low-frequency pulsations of the recirculation bubble accompanied by flapping motions of the shear layer. It is found that the velocity field in the initial part of the interaction, upstream of the corner, is distorted significantly during the low-frequency motions. The flow undergoes low-frequency changes of topology in this region, including the breaking-up of the recirculation bubble. In addition, the development of energetic turbulent structures in the shear layer is observed to be modulated at low frequency, and this could imply a modulation of the shear layer entrainment rate. Concerning the driving mechanism for the unsteadiness, we conjecture that the observed response of the STBLI system could be linked to a global instability in the downstream separated flow. The low-frequency motions in the present DNS have a signature observed on the C_f. This signature is similar to the one obtained in the global unstable mode found by Touber & Sandham (2009). The incoming boundary layer has a weak influence on the

https://doi.org/10.1017/jfm.2011.560 Published online by Cambridge University Press

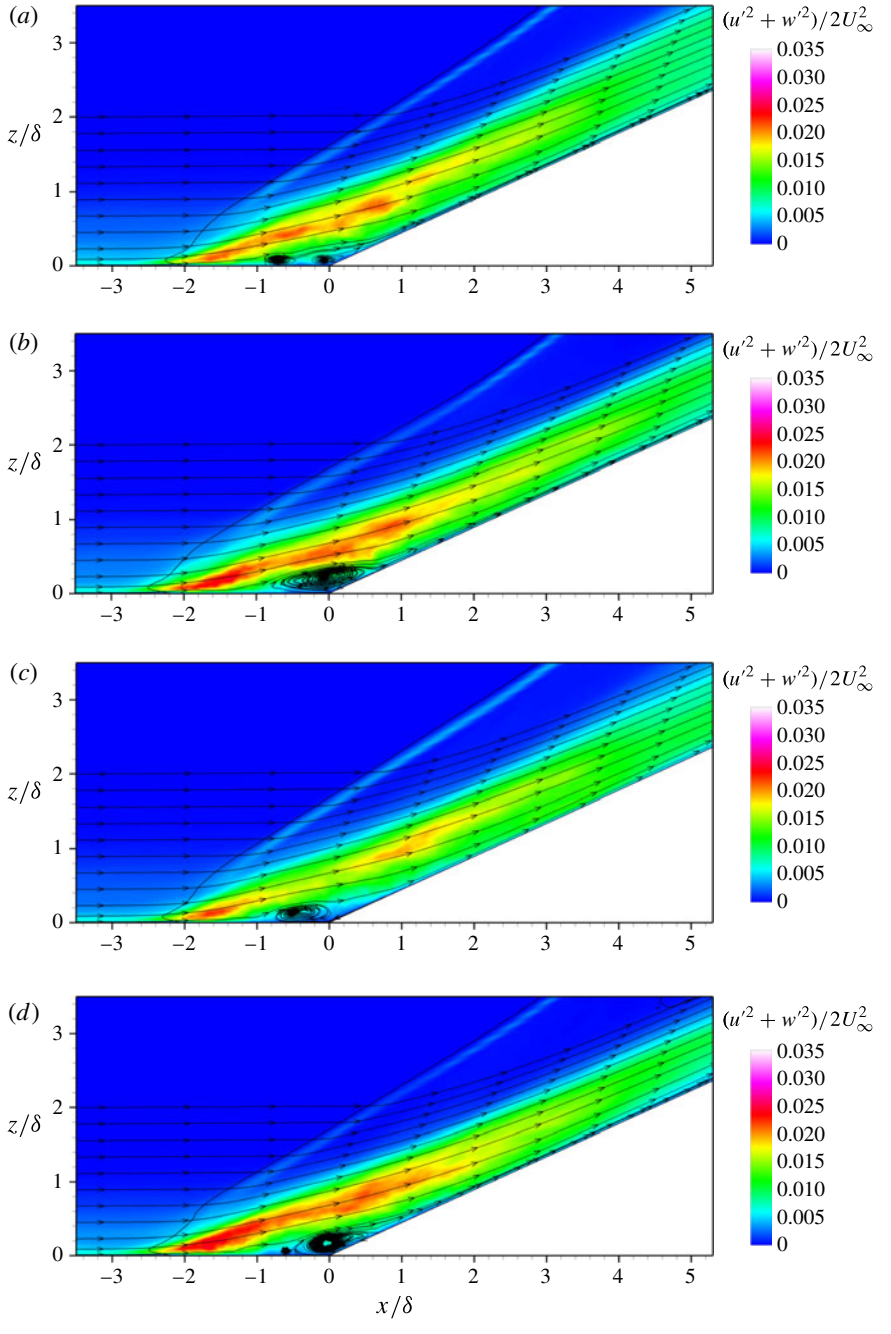


FIGURE 39. Spanwise-averaged low-pass filtered flow fields at the instants indicated in figure 38. The in-plane turbulent kinetic energy $(u'^2 + w'^2)/2U_\infty^2$ is calculated using high-pass filtered velocity fluctuations u' and w'. See text for details.

https://doi.org/10.1017/jfm.2011.560 Published online by Cambridge University Press

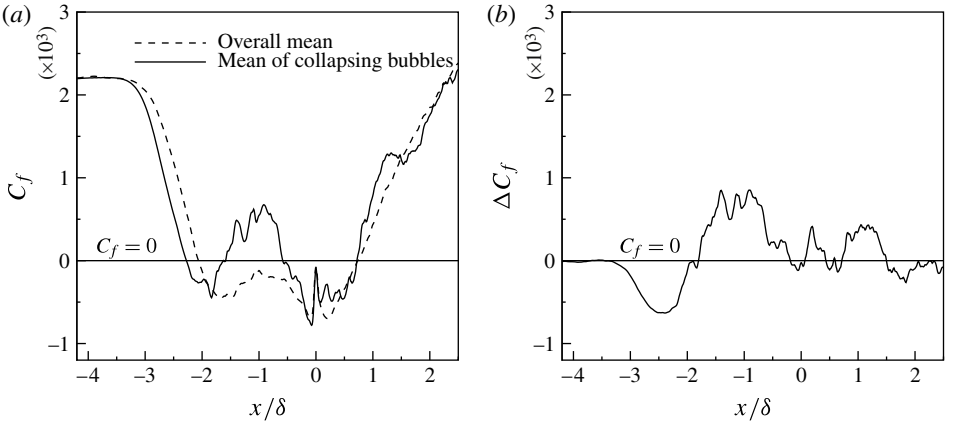


FIGURE 40. (*a*) Overall mean C_f distribution and mean of the collapsing bubble cases shown in figures 29(*c*) and 36(*a*,*c*). (*b*) The difference between the two distributions shown in (*a*).

unsteadiness, either by affecting the shock directly, or by modulating the downstream mechanism, or both.

The present findings may be reconciled with the findings of Ganapathisubramani *et al.* (2007, 2009) and Humble *et al.* (2009*a*), who found significant upstream influence and concluded that the incoming boundary layer is at the origin of the low-frequency unsteadiness. They looked at more weakly separated interactions – the interaction investigated by Humble *et al.* (2009*a*) appears to be incipiently, or possibly very weakly, separated. It may be expected that, in weakly or incipiently separated interactions, upstream perturbations become more important. In other words, it may be expected that the relative importance of the low-frequency dynamics of the separated flow as compared to the importance of the upstream flow is dependent on the degree of separation and hence the interaction strength. In this view, which was suggested by Clemens & Narayanaswamy (2009) and Souverein *et al.* (2010), both upstream and downstream effects are always present, but their relative importance is dependent on the degree of separation and hence on the interaction strength. Downstream effects dominate for fully separated cases, but upstream effects are expected to become relatively more important for mild interactions.

Acknowledgements

This work was supported by the Air Force Office of Scientific Research under grant number AF 9550-09-1-0464. The authors would like to thank Y.-C. Kan for helping to prepare the movies and associated figures in §§ 3.4 and 3.5.

Supplementary movies are available at journals.cambridge.org/flm.

REFERENCES

BENDAT, J. S. & PIERSOL, A. G. 2000 *Random Data: Analysis and Measurement Procedures*, 3rd edn. Wiley.

BENIGNUS, V. A. 1969 Estimation of the coherence spectrum and its confidence interval using the fast Fourier transform. *IEEE Trans. Audio Electroacoust.* **AU-17** (2), 145–150.

https://doi.org/10.1017/jfm.2011.560 Published online by Cambridge University Press

BERESH, S. J., CLEMENS, N. T. & DOLLING, D. S. 2002 Relationship between upstream turbulent boundary-layer velocity fluctuations and separation shock unsteadiness. *AIAA J.* **40** (12), 2412–2422.

BORTEL, R. & SOVKA, P. 2007 Approximation of statistical distribution of magnitude squared coherence estimated with segment overlapping. *Signal Process.* **87** (5), 1100–1117.

CHERRY, N. J., HILLIER, R. & LATOUR, M. E. M. P. 1984 Unsteady measurements in a separated and reattaching flow. *J. Fluid Mech.* **144**, 13–46.

CLEMENS, N. T. & NARAYANASWAMY, V. 2009 Shock/turbulent boundary layer interactions: Review of recent work on sources of unsteadiness. In *39th AIAA Fluid Dynamics Conference*, *AIAA Paper* 2009-3710.

DEBIÈVE, J.-F. & DUPONT, P. 2009 Dependence between the shock and the separation bubble in a shock wave boundary layer interaction. *Shock Waves* **19** (6), 499–506.

DÉLERY, J. & MARVIN, J. G. 1986 Shock-wave boundary layer interactions. *AGARDograph* 280.

DOLLING, D. S. 2001 Fifty years of shock-wave/boundary-layer interaction research: What next? *AIAA J.* **39** (8), 1517–1531.

DUPONT, P., HADDAD, C. & DEBIÈVE, J. F. 2006 Space and time organization in a shock-induced separated boundary layer. *J. Fluid Mech.* **559**, 255–277.

DUPONT, P., PIPONNIAU, S., SIDORENKO, A. & DEBIÈVE, J. F. 2008 Investigation by particle image velocimetry measurements of oblique shock reflection with separation. *AIAA J.* **46** (6), 1365–1370.

DUSSAUGE, J.-P., DUPONT, P. & DEBIÈVE, J.-F. 2006 Unsteadiness in shock wave boundary layer interactions with separation. *Aerosp. Sci. Technol.* **10** (2), 85–91.

EATON, J. K. & JOHNSTON, J. P. 1982 Low frequency unsteadiness of a reattaching turbulent shear layer. In *Turbulent Shear Flows 3* (ed. L. J. S. Bradbury, F. Durst, B. E. Launder, F. W. Schmidt & J. H. Whitelaw), pp. 162–170. Springer.

ERENGIL, M. E. & DOLLING, D. S. 1991 Unsteady wave structure near separation in a Mach 5 compression ramp interaction. *AIAA J.* **29** (5), 728–735.

GANAPATHISUBRAMANI, B., CLEMENS, N. T. & DOLLING, D. S. 2006 Large-scale motions in a supersonic turbulent boundary layer. *J. Fluid Mech.* **556**, 271–282.

GANAPATHISUBRAMANI, B., CLEMENS, N. T. & DOLLING, D. S. 2007 Effects of upstream boundary layer on the unsteadiness of shock-induced separation. *J. Fluid Mech.* **585**, 369–394.

GANAPATHISUBRAMANI, B., CLEMENS, N. T. & DOLLING, D. S. 2009 Low-frequency dynamics of shock-induced separation in a compression ramp interaction. *J. Fluid Mech.* **636**, 397–425.

GREEN, J. E. 1970 Reflexion of an oblique shock wave by a turbulent boundary layer. *J. Fluid Mech.* **40** (1), 81–95.

HOU, Y. X., CLEMENS, N. T. & DOLLING, D. S. 2003 Wide-field PIV study of shock-induced turbulent boundary layer separation. In *41st AIAA Aerospace Sciences Meeting and Exhibit*, *AIAA Paper* 2003-441.

HUMBLE, R. A., ELSINGA, G. E., SCARANO, F. & VAN OUDHEUSDEN, B. W. 2009*a* Three-dimensional instantaneous structure of a shock wave/turbulent boundary layer interaction. *J. Fluid Mech.* **622**, 33–62.

HUMBLE, R. A., SCARANO, F. & VAN OUDHEUSDEN, B. W. 2009*b* Unsteady aspects of an incident shock wave/turbulent boundary layer interaction. *J. Fluid Mech.* **635**, 47–74.

HUTCHINS, N. & MARUSIC, I. 2007 Evidence of very long meandering features in the logarithmic region of turbulent boundary layers. *J. Fluid Mech.* **579**, 1–28.

JIANG, G.-S. & SHU, C.-W. 1996 Efficient implementation of weighted ENO schemes. *J. Comput. Phys.* **126** (1), 202–228.

KIYA, M. & SASAKI, K. 1983 Structure of a turbulent separation bubble. *J. Fluid Mech.* **137**, 83–113.

KIYA, M. & SASAKI, K. 1985 Structure of large-scale vortices and unsteady reverse flow in the reattaching zone of a turbulent separation bubble. *J. Fluid Mech.* **154**, 463–491.

LEE, I. & SUNG, H. J. 2002 Multiple-arrayed pressure measurement for investigation of the unsteady flow structure of a reattaching shear layer. *J. Fluid Mech.* **463**, 377–402.

MARTÍN, M. P. 2007 Direct numerical simulation of hypersonic turbulent boundary layers. Part 1. Initialization and comparison with experiments. *J. Fluid Mech.* **570**, 347–364.

https://doi.org/10.1017/jfm.2011.560 Published online by Cambridge University Press

MARTÍN, M. P., TAYLOR, E. M., WU, M. & WEIRS, V. G. 2006 A bandwidth-optimized WENO scheme for the effective direct numerical simulation of compressible turbulence. *J. Comput. Phys.* **220** (1), 270–289.

NA, Y. & MOIN, P. 1998 Direct numerical simulation of a separated turbulent boundary layer. *J. Fluid Mech.* **374**, 379–405.

PIPONNIAU, S., DUSSAUGE, J. P., DEBIÈVE, J. F. & DUPONT, P. 2009 A simple model for low-frequency unsteadiness in shock-induced separation. *J. Fluid Mech.* **629**, 87–108.

PRIEBE, S. & MARTÍN, M. P. 2009 Analysis of low-frequency unsteadiness in the direct numerical simulation of a shockwave and turbulent boundary layer interaction. In *39th AIAA Fluid Dynamics Conference*, *AIAA Paper* 2009-3711.

PRIEBE, S., WU, M. & MARTÍN, M. P. 2009 Direct numerical simulation of a reflected-shock-wave/turbulent-boundary-layer interaction. *AIAA J.* **47** (5), 1173–1185.

RINGUETTE, M. J., BOOKEY, P., WYCKHAM, C. & SMITS, A. J. 2009 Experimental study of a Mach 3 compression ramp interaction at $Re_\theta = 2400$. *AIAA J.* **47** (2), 373–385.

RINGUETTE, M. J., WU, M. & MARTÍN, M. P. 2008*a* Low Reynolds number effects in a Mach 3 shock/turbulent-boundary-layer interaction. *AIAA J.* **46** (7), 1884–1887.

RINGUETTE, M. J., WU, M. & MARTÍN, M. P. 2008*b* Coherent structures in direct numerical simulation of turbulent boundary layers at Mach 3. *J. Fluid Mech.* **594**, 59–69.

SETTLES, G. S., FITZPATRICK, T. J. & BOGDONOFF, S. M. 1979 Detailed study of attached and separated compression corner flow fields in high Reynolds number supersonic flow. *AIAA J.* **17** (6), 579–585.

SIMENS, M. P., JIMÉNEZ, J., HOYAS, S. & MIZUNO, Y. 2009 A high-resolution code for turbulent boundary layers. *J. Comput. Phys.* **228** (11), 4218–4231.

SMITS, A. J. & DUSSAUGE, J.-P. 2006 *Turbulent Shear Layers in Supersonic Flow*, 2nd edn. Springer.

SOUVEREIN, L. J., DUPONT, P., DEBIÈVE, J.-F., DUSSAUGE, J.-P., VAN OUDHEUSDEN, B. W. & SCARANO, F. 2010 Effect of interaction strength on unsteadiness in turbulent shock-wave-induced separations. *AIAA J.* **48** (7), 1480–1493.

TAYLOR, E. M., WU, M. & MARTÍN, M. P. 2007 Optimization of nonlinear error for weighted essentially non-oscillatory methods in direct numerical simulations of compressible turbulence. *J. Comput. Phys.* **223** (1), 384–397.

THOMAS, F. O., PUTNAM, C. M. & CHU, H. C. 1994 On the mechanism of unsteady shock oscillation in shock wave/turbulent boundary layer interactions. *Exp. Fluids* **18** (1–2), 69–81.

TOUBER, E. & SANDHAM, N. D. 2009 Large-eddy simulation of low-frequency unsteadiness in a turbulent shock-induced separation bubble. *Theor. Comput. Fluid Dyn.* **23** (2), 79–107.

WILLIAMSON, J. H. 1980 Low-storage Runge–Kutta schemes. *J. Comput. Phys.* **35** (1), 48–56.

WU, M. & MARTÍN, M. P. 2007 Direct numerical simulation of supersonic turbulent boundary layer over a compression ramp. *AIAA J.* **45** (4), 879–889.

WU, M. & MARTÍN, M. P. 2008 Analysis of shock motion in shockwave and turbulent boundary layer interaction using direct numerical simulation data. *J. Fluid Mech.* **594**, 71–83.

XU, S. & MARTÍN, M. P. 2004 Assessment of inflow boundary conditions for compressible turbulent boundary layers. *Phys. Fluids* **16** (7), 2623–2639.

https://doi.org/10.1017/jfm.2011.560 Published online by Cambridge University Press